View metadata, citation and similar papers at core.ac.uk

brought to you by CORE

provided by DSpace@MIT

The Astrophysical Journal, 835:81 (22pp), 2017 January 20 doi:10.3847/1538-4357/835/1/81

© 2017. The American Astronomical Society. All rights reserved.

BRIGHT METAL-POOR STARS FROM THE HAMBURG/ESO SURVEY. II. A CHEMODYNAMICAL ANALYSIS

Timothy C. Beers[1], Vinicius M. Placco[1], Daniela Carollo[1], Silvia Rossi[2], Young Sun Lee[3], Anna Frebel[4], John E. Norris[5], Sarah Dietz[1], and Thomas Masseron[6]

[1] Department of Physics and JINA Center for the Evolution of the Elements, University of Notre Dame, Notre Dame, IN 46556, USA; tbeers@nd.edu, vplacco@nd.edu, dcarollo@nd.edu, sdietz@nd.edu

[2] Instituto de Astronomia, Geofísica e Ciências Atmosféricas, Departamento de Astronomia, Universidade de São Paulo, Rua do Matão 1226, 05508-900 São Paulo, Brazil; rossi@astro.iag.usp.br

[3] Department of Astronomy & Space Science, Chungnam National University, Daejeon 34134, Korea; youngsun@cnu.ac.kr

[4] Massachussetts Institute of Technology and Kavli Institute for Astrophysics and Space Research, 77 Massachusetts Avenue, Cambridge, MA, 02139, USA; afrebel@mit.edu

[5] Research School of Astronomy and Astrophysics, The Australian National University, Mount Stromlo Observatory, Cotter Road, Weston, ACT 2611, Australia; john.norris@anu.edu.au

[6] Institute of Astronomy, University of Cambridge, Madingley Road, CB3 0HA, Cambridge, UK; tpm40@ast.cam.ac.uk

Received 2016 September 28; revised 2016 November 9; accepted 2016 November 11; published 2017 January 19

ABSTRACT

We obtain estimates of stellar atmospheric parameters for a previously published sample of 1777 relatively bright ($9 < B < 14$) metal-poor candidates from the Hamburg/ESO Survey. The original Frebel et al. analysis of these stars was able to derive estimates of [Fe/H] and [C/Fe] only for a subset of the sample, due to limitations in the methodology then available. A new spectroscopic analysis pipeline has been used to obtain estimates of $T_{\rm eff}$, log g, [Fe/H], and [C/Fe] for almost the entire data set. This sample is very local—about 90% of the stars are located within 0.5 kpc of the Sun. We consider the chemodynamical properties of these stars in concert with a similarly local sample of stars from a recent analysis of the Bidelman and MacConnell "weak metal" candidates by Beers et al. We use this combined sample to identify possible members of the halo stream of stars suggested by Helmi et al. and Chiba & Beers, as well as stars that may be associated with stripped debris from the putative parent dwarf of the globular cluster Omega Centauri, suggested to exist by previous authors. We identify a clear increase in the cumulative frequency of carbon-enhanced metal-poor (CEMP) stars with declining metallicity, as well as an increase in the fraction of CEMP stars with distance from the Galactic plane, consistent with previous results. We also identify a relatively large number of CEMP stars with kinematics consistent with the metal-weak thick-disk population, with possible implications for its origin.

Key words: Galaxy: kinematics and dynamics – Galaxy: stellar content – stars: abundances – stars: carbon – stars: Population II – stars: kinematics and dynamics

Supporting material: machine-readable tables

1. INTRODUCTION

There have been numerous recent studies of the disk system of the Milky Way, primarily based on data from the Sloan Digital Sky Survey (SDSS; York et al. 2000), in particular the SEGUE (Yanny et al. 2009) and APOGEE (Majewski et al. 2015) sub-surveys, as well as from the Radial Velocity Experiment (RAVE; Steinmetz et al. 2006; Kordopatis et al. 2013) and the *Gaia*-ESO survey (Gilmore et al. 2012; Guiglion et al. 2015). Beers et al. (2014) and Guiglion et al. (2015) summarize the pertinent papers, to which the interested reader is referred. Most of these papers model the Galactic disk system in terms of a superposition of a thin disk, a thick disk, and (in some cases) a metal-weak thick disk (MWTD). The series of papers from Bovy and collaborators, culminating with Bovy et al. (2015), has taken a different approach. These authors use abundance information ([Fe/H] and [α/Fe]) for large samples of red-clump stars measured with APOGEE to model the radial and vertical structure of the disk in terms of mono-abundance populations (MAPs), and demonstrate that this technique captures the relevant observations without invoking a separation of stellar populations. Because MAPs are based on red-clump stars, they do not include any stars with [Fe/H] < -1.0 and so are not suitable for exploring issues relating to the MWTD, which Beers et al. (2014) have argued to be a potentially separate component of the disk system that has yet to be explored in detail. A recent paper by Kawata & Chiappini (2016) emphasizes that the separability of the thin disk and thick disk remains uncertain, arguing that the scheme of chemically dividing the disk system on the basis of the [α/Fe] ratio, pioneered by Lee et al. (2011a, 2011b), is for now the most practical approach.

One of the first large spectroscopic samples of stars in the disk system was originally reported by Frebel et al. (2006; hereafter, Paper I). These stars, selected from partially saturated objective-prism spectra from the Hamburg/ESO survey (HES; Wisotzki et al. 2000; Christlieb 2003) with $9 < B < 14$, formed the basis of an early effort to identify bright metal-poor halo stars in the Galaxy. Due to flaws in the selection procedure, the great majority of these stars turned out to have metallicities more typical of the disk system than of the halo. Even so, the star HE 1327-2326, which was first identified in that effort, turned out to have one of the lowest iron abundance known ([Fe/H] $= -5.45$; Frebel et al. 2005; Aoki et al. 2006), only recently surpassed by SMSS J031300.36−670839.31, with [Fe/H] < -7.8 (Keller et al. 2014; Bessell et al. 2015). That paper was also the first to suggest an increase in the fraction of carbon-enhanced metal-poor (CEMP) stars (Beers & Christlieb 2005) with distance from the Galactic plane, which was later

confirmed with much larger samples of stars from SDSS (Carollo et al. 2012).

A substantial fraction of very low metallicity stars in the halo of the Milky Way have been found to be CEMP stars. Beers & Christlieb (2005) originally divided such stars into several sub-classes, depending on the nature of their neutron-capture element abundance ratios—CEMP-*s*, CEMP-*r*, CEMP-*r*/*s*, and CEMP-no.[7] As discussed by those authors and many others since, the observed differences in the chemical signatures of the sub-classes of CEMP stars are thought to arise from differences in the astrophysical sites responsible for the nucleosynthesis products they now incorporate in their atmospheres, including elements produced by the very first generations of stars.

At the time Paper I was published, the authors could obtain estimates of [Fe/H] and [C/Fe] from their spectra only for those stars with [Fe/H] < -1.0, due to the nascent saturation of the Ca II K line. This limitation precluded a comprehensive investigation of the disk system, including stars over the full range of expected metallicities. Over the course of the past decade, we have developed and tested new spectroscopic tools (primarily for application to SDSS stellar spectra—the SEGUE Stellar Parameter Pipeline, SSPP) that are useful for the analysis of stars over wide ranges of [Fe/H] (see, e.g., Lee et al. 2008a). In this paper, we employ a modification of the SSPP that can be used for spectra of similar resolving power and with input broadband V, $B-V$ and/or J, $J-K$ photometry, to obtain estimates of the stellar atmospheric parameters $T_{\rm eff}$, log g, and [Fe/H], as well as [C/Fe] abundance ratios for most of the stars in the Paper I sample. Similarly determined quantities from the local sample of "metal-weak" candidates from Bidelman & MacConnell (1973), reported recently by Beers et al. (2014), are analyzed in concert with the Paper I sample.

This information (in combination with well-determined radial velocities and available accurate proper motions) is employed to carry out a detailed examination of the kinematics of the combined sample and identify stars that are possible members of the halo stream/trail of stars by Helmi et al. (1999) and Chiba & Beers (2000), as well as stars that may be associated with stripped debris from the putative parent dwarf of the globular cluster Omega Centauri (ω Cen), suggested to exist by Dinescu (2002), Klement et al. (2009), and Majewski et al. (2012). We identify a clear increase in the cumulative frequency of CEMP stars as a function of declining metallicity, as well as an increase in the fraction of CEMP stars with distance from the Galactic plane, as quantified by the maximum distances reached during the course of their orbits, $Z_{\rm max}$, both consistent with previous results. We also identify a number of CEMP stars that are apparently associated with the MWTD, with implications for its origin. Finally, we make use of the Yoon–Beers diagram of A(C) versus [Fe/H] (Figure 1 of Yoon et al. 2016) to sub-classify the relatively small number of CEMP stars in the combined sample with available kinematic information (36 stars) into likely CEMP-*s* and CEMP-no stars, and show that the distributions of their $Z_{\rm max}$ differ, in the sense that the CEMP-*s* stars appear to be preferentially associated with the inner-halo population, while the CEMP-no stars are more likely to be associated with the outer-halo population, similar to the previous claim of Carollo et al. (2014).

[7] CEMP-*s*: [C/Fe] $> +1.0$, [Ba/Fe] $> +1.0$, and [Ba/Eu] $> +0.5$; CEMP-*r*: [C/Fe] $> +1.0$ and [Eu/Fe] $> +1.0$; CEMP-*r*/*s*: [C/Fe] $> +1.0$ and $0.0 <$ [Ba/Eu] $< +0.5$; CEMP-no: [C/Fe] $> +1.0$ and [Ba/Fe] < 0.0.

2. SAMPLE STARS AND ADOPTED PHOTOMETRY

Paper I describes the original motivations and selection of the bright candidate metal-poor stars from the HES, to which the interested reader is referred for details. Unfortunately, the original candidate selection was confounded by (known) saturation effects on the derived estimates of approximate $B-V$ to such a degree that numerous stars were included that later turned out to be more metal-rich than hoped for. In spite of this limitation, more than a hundred relatively bright very metal-poor (VMP; [Fe/H] < -2.0) stars were identified during follow-up spectroscopy, which formed the basis for much of the analysis carried out in Paper I.

In the present paper, we re-analyze medium-resolution ($R \sim 2000$) spectroscopy of the sample of stars from Paper I (see Table 6 of Paper I for the telescope/spectrographs employed), using the n-SSPP spectroscopic pipeline described below. This new effort, which also incorporates a large amount of newly available broadband V, $B-V$ photometry for the sample stars, enables determinations of stellar atmospheric parameters for the great majority of the Paper I sample, including stars with metallicities up to solar and beyond (which were not previously possible), as well as refined estimations of [C/Fe] abundance ratios for most of the stars in this sample.

2.1. Broadband Photometry and Reddening Estimation

Broadband V magnitudes and $B-V$ colors for the majority of our program objects were obtained from the APASS database (Henden et al. 2015), supplemented by photometry from a number of sources as described in Paper I (primarily stars that were re-discoveries of metal-poor candidates from the HK survey; Beers et al. 1985, 1992). For stars that are of particular interest, i.e., those found in Paper I to have [Fe/H] < -2.0 or to exhibit enhanced carbon, we also make use of photometry reported by Beers et al. (2007). In a number of cases, we have also used photometry from the SIMBAD database. For stars with photometry available from multiple sources, we either use the data judged to be superior, or else average data expected to be of similar precision. Near-IR *JHK* photometry from the 2MASS catalog (Skrutskie et al. 2006) is available for all but a few stars in our sample.

Column (1) of Table 1 lists the star names, while columns (2) and (3) list other common names for the star and the HK Survey star name, respectively. The full set of coordinates for our program stars are provided in Paper I. Columns (4) and (5) list the Galactic longitude and latitude for our program stars. The adopted V magnitude and $B-V$ colors are provided in columns (6) and (7). The 2MASS J magnitude and $J-K$ colors (including only stars without flags indicating potential problems in the listed values) are listed in columns (8) and (9).

In order to obtain absorption- and reddening-corrected estimates of the magnitudes and colors, respectively, we initially adopted the Schlegel et al. (1998) estimates of reddening listed in column (10) of Table 1. We have applied corrections to these estimates for stars with reddening greater than $E(B-V)_S = 0.10$, as described by Beers et al. (2000). The corrected reddening estimates, $E(B-V)_A$, are listed in column (11).

Table 1
Photometric Information and Adopted Reddening

Star Name	Other Name	HK Survey	LON (°)	LAT (°)	V (mag)	$B-V$ (mag)	J (mag)	$J-K$ (mag)	$E(B-V)_S$ (mag)	$E(B-V)_A$ (mag)
(1)	(2)	(3)	(4)	(5)	(6)	(7)	(8)	(9)	(10)	(11)
HE 0000-3017	CD-30:19801		14.8	−79.1	10.36	0.40	9.546	0.275	0.015	0.02
HE 0000-4401	CD-44:15435		330.2	−70.7	10.66	0.55	9.717	0.302	0.010	0.01
HE 0000-5703	HD 225032		315.9	−59.1	9.40	0.24	9.001	0.109	0.010	0.01
HE 0001-4157	CD-42:16578		333.7	−72.5	10.52	0.67	9.385	0.376	0.012	0.01
HE 0001-4449	CD-45:15231		328.4	−70.2	11.14	0.49	10.192	0.296	0.012	0.01
HE 0001-5640	CD-57:8943		315.9	−59.5	10.50	0.41	9.571	0.285	0.011	0.01
HE 0002-3233		CS 22961-023	2.9	−78.8	12.00	0.41	11.068	0.323	0.016	0.02
HE 0002-3822	CD-38:15729		341.8	−75.3	10.79	0.53	9.808	0.335	0.016	0.02
HE 0002-5625			315.9	−59.8	12.60	0.69	11.425	0.424	0.010	0.01
HE 0003-0503	BD-05:6112		95.0	−65.2	10.70	0.74	8.990	0.602	0.030	0.03

(This table is available in its entirety in machine-readable form.)

3. RADIAL VELOCITIES, LINE INDICES, ATMOSPHERIC PARAMETERS, ABUNDANCE RATIOS, DISTANCES, AND PROPER MOTIONS

3.1. Measurement of Radial Velocities and Line Indices

Radial velocities were (re-)measured for our program stars using the line-by-line and cross-correlation techniques described in detail by Beers et al. (1999) and references therein. In the process of carrying out this exercise, we found that many of the new measurements differ (in some cases by large amounts) from those originally reported in Paper I, which apparently suffered from transcription difficulties during file exchanges between the authors. The current measurements supersede those values. The spectral resolution of our data is similar to that obtained for the majority of the HK Survey follow-up; thus we expect that the measured radial velocities should be precise to the same level (or better, given the higher signal-to-noise of our present spectra), on the order of 7–10 km s^{-1} (one sigma). Column (1) of Table 2 is the star name, while column (2) lists notes on the nature of a small number of stars that deviate from the majority (e.g., hot stars, sdB and WD stars, known variable stars, stars with emission lines, extremely late-type stars), which precludes their use in later analysis. We conservatively estimate that our medium-resolution velocities, RV_M, listed in column (3) of Table 2, are precise to 10 km s^{-1} (as validated below).

Roughly one-third of our program objects (614 stars) have had radial velocities determined from the RAVE survey, based on moderate-resolution ($R \sim 7500$) spectroscopy in the region of the Ca triplet from Data Release 4 (Kordopatis et al. 2013). The RAVE velocities should be more precise than those we obtained from our lower-resolution spectra (Kordopatis et al. 2013 demonstrate that the majority of the RAVE radial velocities are precise to better than 2 km s^{-1}, with a tail going out to ∼5 km s^{-1}, and have small zero-point offsets relative to external catalogs). For our purpose we conservatively assume a precision of 5 km s^{-1} for the RAVE velocities (validated below). We adopt the RAVE velocities for our subsequent analysis, except in cases where flags were raised in the DR4 database indicating potential problems (including possible binary membership). The available RAVE velocities are listed as RV_R in column (4) of Table 2. In order to weed out stars with inaccurate RAVE velocities, we have indicated stars with flags suggesting potential problems with parentheses around them. We still adopt these radial velocities for our analysis if they are within 20 km s^{-1} of the listed RV_M value. If the RAVE velocities differ by more than this amount and had flags raised, we assume that the RV_M estimates are superior. We indicate such cases by brackets around the listed RV_R values. In some instances, there are no flags raised, but the RAVE radial velocities differ from our medium-resolution results by more than 20 km s^{-1}; in such cases, we assume the RAVE estimates are superior, and adopt them.

There are 148 stars in our sample (mostly VMP stars and stars of interest for other reasons, such as carbon enhancement) for which radial velocities based on high-resolution spectroscopy are available, either in the published literature or based on more recent unpublished observations we are aware of. These are listed as RV_H in column (5) of Table 2. We adopt these measurements (when available), with assumed errors of 2 km s^{-1}, even in the few cases where they disagree by more than 20 km s^{-1} with either RV_M or RV_R. Unrecognized binarity may be responsible for a number of these discrepancies.

Figure 1 (left column) compares the medium-resolution velocities, RV_M, with the high-resolution radial velocities, RV_H, while the middle column of panels compares RV_M with the moderate-resolution RAVE velocities, RV_R (excluding the rejected cases). The right column of panels compares the RAVE velocities with the high-resolution velocities. As can be appreciated from inspection of this figure, there is generally very good agreement between the different sources of radial velocity. The middle row of panels shows the residuals in radial velocity for each comparison, with dark gray and light gray regions indicating the 1σ and 2σ ranges, respectively. Maximum-likelihood fits to the residuals in radial velocity for each comparison are shown in the lower panels of each column. The RV_M versus RV_H residuals exhibit a scatter of 10.7 km s^{-1} and a small zero-point offset; the RV_M versus RV_R residuals exhibit a scatter of 8.8 km s^{-1} and a similarly small offset. The RV_R versus RV_H residuals exhibit a scatter of 4.7 km s^{-1} and a small offset. Assuming our adopted estimate of the 2 km s^{-1} precision for the high-resolution radial velocities, our results indicate that the RAVE radial velocities are precise to 4.2 km s^{-1} (note that this comparison emphasizes metal-poor stars, for which the RAVE velocities are expected to be somewhat less precise than for more metal-rich stars). Adopting this value for the scatter in the RAVE velocities, we estimate that the medium-resolution velocities have a precision of 7.7 km s^{-1}. Compared to the high-resolution velocities, the medium-resolution velocities are estimated to

Table 2
Radial Velocities, Line Indices, Atmospheric Parameters, and Type Assignments

Star Name	Note	RV_M (km s^{-1})	RV_R (km s^{-1})	RV_H (km s^{-1})	KP (Å)	HP2 (Å)	GP (Å)	$Teff_S$ (K)	log g_S (cgs)	$[Fe/H]_S$	$Teff_R$ (K)	log g_R (cgs)	$[Fe/H]_R$	$Teff_H$ (K)	log g_H (cgs)	$[Fe/H]_H$	$Teff_C$ (K)	log g_C (cgs)	$[Fe/H]_C$	TYPE
(1)	(2)	(3)	(4)	(5)	(6)	(7)	(8)	(9)	(10)	(11)	(12)	(13)	(14)	(15)	(16)	(17)	(18)	(19)	(20)	(21)
HE 0000-3017		21.8	...	...	6.57	4.99	1.89	6666	3.99	−0.18	...	...	...	6875	4.60	+0.23	6776	4.41	+0.20	D
HE 0000-4401		−1.0	−2.1	...	8.29	3.60	3.55	6199	3.77	−0.13	6168	4.12	−0.05	...	...	...	6227	4.14	+0.26	D
HE 0000-5703		30.3	26.4	...	2.59	9.37	1.16	7758	4.08	−0.03	7474	4.25	−0.10	...	...	...	8060	4.53	+0.30	D
HE 0001-4157		2.0	−10.8	...	9.15	1.73	5.47	5725	3.81	−0.10	5710	3.99	+0.10	...	...	...	5670	4.19	+0.30	D
HE 0001-4449		5.0	−9.4	...	7.53	3.53	2.92	6227	3.65	−0.58	5959	3.66	−0.62	...	...	...	6260	3.99	−0.28	TO
HE 0001-5640		−14.0	[23.3]	...	7.80	4.06	2.82	6377	3.86	−0.26	6176	3.65	+0.14	...	...	...	6436	4.25	+0.11	D
HE 0002-3233		61.1	...	...	1.30	4.24	0.48	6349	3.65	−2.54	...	...	...	...	...	...	6404	4.00	−2.70	TO
HE 0002-3822		−8.0	...	...	7.80	3.39	3.20	6132	3.87	−0.59	...	...	...	...	...	...	6148	4.26	−0.30	D
HE 0002-5625		22.4	...	...	9.25	1.65	5.55	5750	4.02	−0.14	...	...	...	...	...	...	5699	4.45	+0.25	D
HE 0003-0503		30.6	34.4	...	6.82	3.39	4.21	5972	2.63	−1.10	(4793)	(3.46)	(−0.19)	...	...	...	5960	2.72	−0.92	G

Note. Parentheses around a listed quantity indicate that it is regarded with some suspicion, while brackets indicate that it is considered as possibly flawed. See text for more details.

(This table is available in its entirety in machine-readable form.)

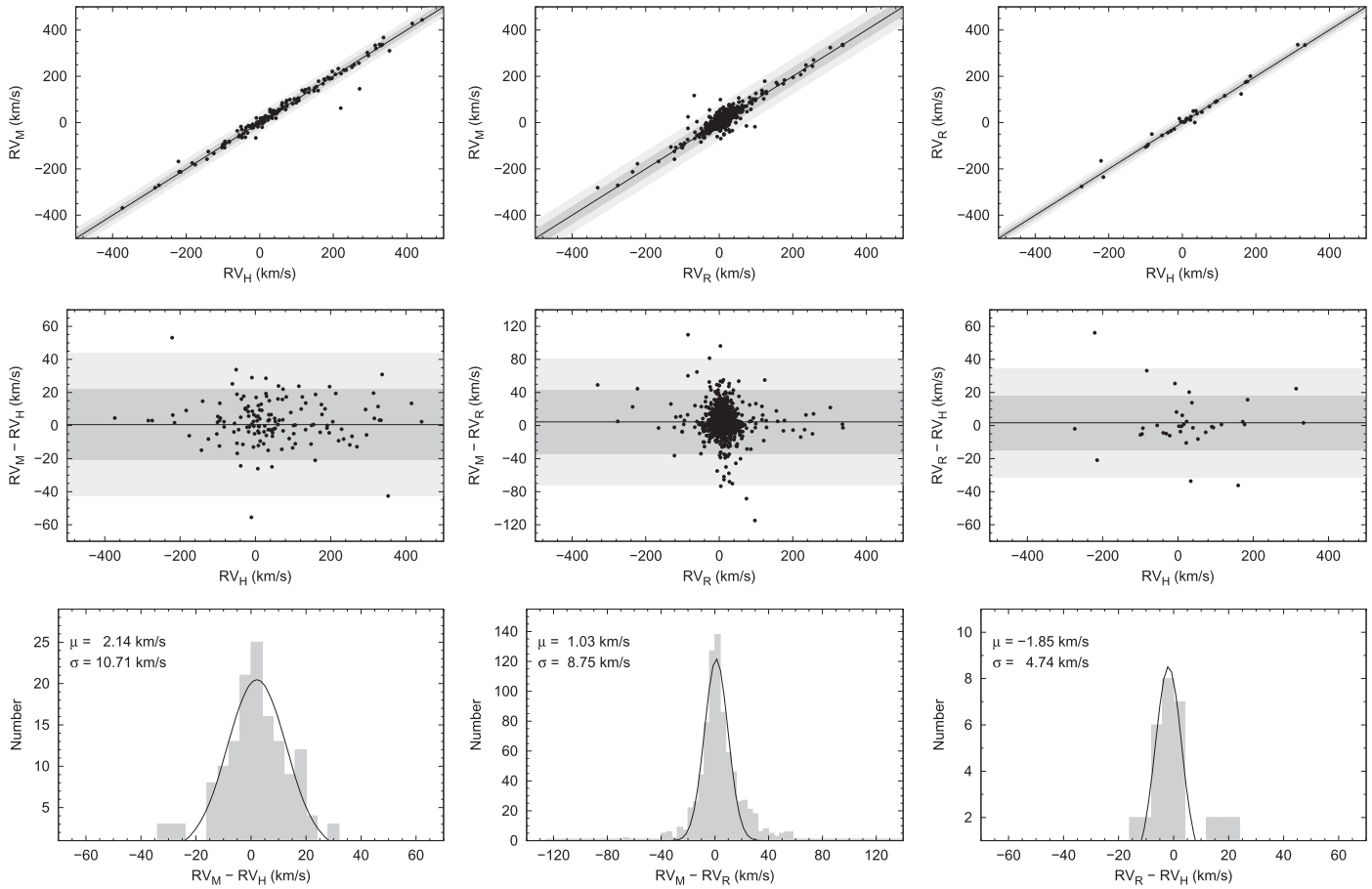

Figure 1. Radial velocity comparison for the program (RV_M), RAVE (RV_R), and high-resolution (RV_H) stars. Upper panels: comparison between the radial velocities. The solid line is the one-to-one line, and the shaded areas represent the 1σ and 2σ intervals around this line (where σ represents the scatter in the residuals shown in the lower panels). Middle panels: residuals between each pair of measurements. The horizontal solid line is the average of the residuals, while the darker and lighter shaded areas represent the 1σ and 2σ regions, respectively. Lower panels: histogram of the residuals in the radial velocity determinations. The values of the mean offset and scatter are the parameters from the Gaussian fit shown.

have a precision of $10.5\,\mathrm{km\,s^{-1}}$. These values justify our adopted estimates for the kinematic analysis carried out below —$\sigma_{RV_R} = 5\,\mathrm{km\,s^{-1}}$ and $\sigma_{RV_M} = 10\,\mathrm{km\,s^{-1}}$ for the RAVE and medium-resolution velocities, respectively.

For each star, the measured (geocentric) radial velocities are used to place a set of fixed bands for the derivation of line-strength indices, which are the pseudo-equivalent widths of prominent spectral features. We employ a subset of the bands listed in Table 1 of Beers et al. (1999).[8] Although we do not make use of them in the present analysis, others may choose to, so we list line indices for prominent spectral features in each of our program stars in columns (6)–(8) of Table 2. A number of our stars have had more than one spectrum obtained during the course of our follow-up observations. From a comparison of the stars with repeated measurements, we estimate that errors in the line indices on the order of 0.1 Å are achieved. Note that our line indices are identical to those reported in Paper I.

3.2. Stellar Atmospheric Parameter Estimates and Abundance Ratios

In a series of papers, Lee et al. (2008a, 2008b, 2011a), Allende Prieto et al. (2008), and Smolinski et al. (2011) describe the development, testing, and validation of the SSPP software, which has been used to determine atmospheric parameter estimates for over 500,000 stars from the SDSS and its extensions. Although the spectra of our program stars do not reach as far red as SDSS spectra (and hence we cannot use as many of the independent methods as the SSPP enables), they are of similar resolving power. We have thus modified the SSPP to accept input from our program spectra, which span a range of 3600–4400 Å, 3600–4800 Å, or 3600–5250 Å, depending on the telescope/spectrograph that was used to acquire them. We have also implemented the use of input V, $B-V$ (and/or 2MASS J, $J-K$) photometric information rather than requiring SDSS *ugriz* inputs. This new approach, known as the n-SSPP (for non-SEGUE Stellar Parameter Pipeline), makes use of a subset of previously calibrated methods from the SSPP (those that apply to the available wavelength range of the input spectra) to obtain estimates of the fundamental stellar parameters $T_{\rm eff}$, log g, and [Fe/H]. For spectra that extend sufficiently redward to include the CH G-band at ∼4300 Å and/or the Mg I feature at ∼5175 Å, the n-SSPP can obtain estimates of [C/Fe] and [α/Fe][9] as well (if the spectra are of sufficiently high signal-to-noise, S/N). The n-SSPP has already been applied by Beers et al. (2014) to

[8] A complete discussion of the choice of bands, the "band-switching" scheme, and the Balmer line index, HP2, which measures the strength of the Hδ lines, is provided in this reference as well.

[9] This notation is usually defined as an average of [Mg/Fe], [Si/Fe], [Ca/Fe], and [Ti/Fe].

Table 3
Carbon Abundance Ratios and Absolute Carbon Abundance Estimates

Star Name (1)	$[Fe/H]_S$ (2)	$[C/Fe]_S$ (3)	DETECT (4)	CC (5)	EQW (6)	$[Fe/H]_C$ (7)	$[C/Fe]_C$ (8)	A(C) (9)	CEMP (10)
HE 0000-3017	−0.18	+0.15	D	0.995	2.33	+0.20	−0.12	8.52	N
HE 0000-4401	−0.13	+0.08	D	0.996	4.14	+0.26	−0.19	8.50	N
HE 0000-5703	−0.03	...	X	...	...	+0.30	...	...	X
HE 0001-4157	−0.10	+0.04	D	0.999	6.42	+0.30	−0.23	8.50	N
HE 0001-4449	−0.58	+0.25	D	0.994	3.26	−0.28	0.00	8.15	N
HE 0001-5640	−0.26	+0.19	D	0.997	3.48	+0.11	−0.07	8.46	N
HE 0002-3233	−2.54	+1.29	D:	0.866	0.76	−2.70	+1.11	6.84	U
HE 0002-3822	−0.59	+0.17	D	0.994	3.66	−0.30	−0.09	8.04	N
HE 0002-5625	−0.14	−0.03	D	0.999	6.71	+0.25	−0.30	8.38	N
HE 0003-0503	−1.10	+1.42	D	0.971	5.20	−0.92	+1.25	8.75	C

Note. A colon following the DETECT code indicates that either the CC or the EQW parameter does not meet the minimum required value for confident detection. See text for more details.

(This table is available in its entirety in machine-readable form.)

medium-resolution spectra of stars from the sample of Bidelman & MacConnell (1973) stars studied by Norris et al. (1985). The interested reader should consult that paper for additional information on the operation of the n-SSPP.

We apply the n-SSPP to the sample of 1777 stars from Paper I. Unfortunately, the S/Ns for the spectra of our program stars that extend to wavelength regions that include the Mg I feature are not generally high enough to enable confident estimation of this abundance ratio (Lee et al. 2011a recommend S/N > 20 or 25, the latter applying to stars with [Fe/H] < −1.4); hence we do not report [α/Fe] for our program stars.

The n-SSPP estimates of stellar atmospheric parameters are listed in columns (9)–(11) of Table 2 as Teff$_S$, log g_S, and $[Fe/H]_S$. Although according to the tests described by Lee et al. (Lee et al. 2008a, 2008b) and Allende Prieto et al. (2008) the external accuracy of SSPP parameter estimates is expected to be on the order of 150 K, 0.30 dex, and 0.25 dex for $T_{\rm eff}$, log g, and [Fe/H], respectively, these are based on the availability of SDSS *ugriz* and the full spectral coverage associated with SDSS spectroscopy, neither of which applies to the present data. We provide an independent test of our expected parameter errors below.

Lee et al. (2013) describes the procedures adopted to estimate [C/Fe] for SDSS/SEGUE spectra, based on spectral matching against a dense grid of synthetic spectra; these techniques, with different input photometric information, also apply to the n-SSPP. We have recently expanded the carbon grid to reach as low as [C/Fe] = −1.5, rather than the limit of [C/Fe] = −0.5 employed by Lee et al. (2013). According to Lee et al., the precision of [C/Fe] estimates is better than 0.35 dex for the parameter space and S/Ns explored by SDSS/SEGUE spectra. We expect improved results for the application of the n-SSPP to our program spectra, based on their generally higher signal-to-noise (which typically exceeds S/N ∼50 in the region of the CH *G*-band). We note that Beers et al. (2014) concluded that the n-SSPP determination of [C/Fe] for spectra with S/N similar to that of our current program achieved a precision (based on empirical comparisons with high-resolution spectroscopic analyses) of ∼0.20 dex.

Table 3 lists the medium-resolution estimates of the [C/Fe] abundance ratios ("carbonicity") for our program stars in column (3), indicated as $[C/Fe]_S$. For convenience, we have also listed the n-SSPP estimate of $[Fe/H]_S$ in column (2). Column (4) indicates whether the listed measurement is considered a detection, DETECT = "D"; a lower limit, "L"; an upper limit, "U"; or a non-detection, "X," which indicates either that the star is too hot (or cool) for carbon to be measured from the CH *G*-band or that the star does not have a reference metallicity determination. Column (5) provides the correlation coefficient, CC, obtained between the observed spectrum and the best-matching [C/Fe] from the model grids, and column (6) lists the equivalent width of the CH *G*-band, EQW. For an acceptable measurement of this ratio, we require DETECT = "D," CC ⩾ 0.7, and EQW ⩾ 1.2. The latter restriction ensures that stars with very weak carbon features are not spuriously assigned values by the grid search procedure. See Lee et al. (2013) for a further discussion of these quantities. Stars for which either the CC or the EQW does not meet the minimum value are indicated by a colon attached to the DETECT parameter in column (4). There are 1491 stars listed in Table 3 for which acceptable measurements of [C/Fe] are obtained—1422 are listed as detections, 58 as upper limits, and 11 as lower limits.

3.3. Comparison to Moderate- and High-resolution Spectroscopic Analyses

There are external measurements of stellar atmospheric parameter estimates for 707 stars in our sample from the RAVE DR4 catalog (Kordopatis et al. 2013) and another 104 stars for which atmospheric parameter estimates based on high-resolution analyses are available from a variety of sources, including the SAGA database (Suda et al. 2008, 2011; Yamada et al. 2013) and Frebel (2010), as well as the references listed in the PASTEL catalog (Soubiran et al. 2010),[10] supplemented by determinations that have appeared in more recent studies, or unpublished results from co-authors of this paper. We either adopted the parameter estimates we judged to be superior or, in some cases, took a straight average of the available estimates.

The external parameter estimates from RAVE are listed in columns (12)–(14) of Table 2 as Teff$_R$, log g_R, and $[Fe/H]_R$. The high-resolution estimates are listed in columns (15)–(17) of that table as Teff$_H$, log g_H, and $[Fe/H]_H$.

[10] We are aware that an updated version of this catalog, Soubiran et al. (2016), is now available, but it was published after we completed the bulk of our analysis, and is hence not used for this exercise.

Before carrying out comparisons with our own estimates, based on medium-resolution spectra, we first check for external parameter estimates that grossly differ from the estimates determined by the n-SSPP. For the external estimates to be considered commensurate with the n-SSPP estimates, reasonable agreement with the effective temperature, $T_{\rm eff}$, is required, at a minimum. To implement this pre-filter, we require that the estimated effective temperatures from the external comparisons are within 500 K of the n-SSPP estimates and (in the case of RAVE) that there be no other indication of potential problems, such as flags raised in the RAVE DR4 catalog listing. This results in a total of 80 stars with RAVE estimates marked as suspect, indicated in Table 2 with brackets around the individual parameter estimates. Only 9 stars with available high-resolution spectroscopic parameter estimates are suspect by this criterion, and these are marked with parentheses around the individual parameter estimates in the table.

Beers et al. (2014) presented a similar analysis for the sample of 302 metal-poor candidates from Bidelman & MacConnell (1973) studied by Norris et al. (1985), roughly one-third of which had external estimates of stellar atmospheric parameters based on high-resolution spectroscopic analyses. Beers et al. used the sample of stars in common to derive empirical corrections to the n-SSPP parameter estimates, which they applied in order to place these estimates on a scale commensurate with that of the high-resolution work. For the convenience of the reader, these corrections are listed below:

$$[{\rm Fe/H}]_C = [{\rm Fe/H}]_S - (-0.232 \cdot [{\rm Fe/H}]_S - 0.428), \quad (1)$$

$$T{\rm eff}_C = T{\rm eff}_S - (-0.1758 \cdot T{\rm eff}_S + 1062), \quad (2)$$

$$\log g_C = \log g_S - (-0.237 \cdot \log g_S + 0.523). \quad (3)$$

The corrected n-SSPP estimates ($T{\rm eff}_C$, $\log g_C$, and $[{\rm Fe/H}]_C$) for our program stars are listed in columns (18)–(20) of Table 2. Column (21) of this table lists our adopted type classifications, obtained as described below.

Figure 2 illustrates comparisons of $T{\rm eff}_C$, $\log g_C$, and $[{\rm Fe/H}]_C$ for our program stars with the adopted high-resolution results. Note that, with the exception of a few individual stars lying outside the 2σ bands shown on the left panels, their agreement is quite satisfactory. Maximum-likelihood fits to the distributions of residuals between these various estimates are shown on the right panels. Both the mean offsets ($\Delta\ T{\rm eff}_C = 117$ K, $\Delta \log g_C = 0.34$ dex, $\Delta\ [{\rm Fe/H}]_C = 0.05$ dex) and the scatter in the estimates ($\sigma\ T{\rm eff}_C = 179$ K, $\sigma \log g_C = 0.65$ dex, $\sigma\ [{\rm Fe/H}]_C = 0.27$ dex) are reasonably small. Taking into account the expected errors in the high-resolution estimates of these parameters (125 K, 0.4 dex, and 0.2 dex, respectively), we conclude that the external precision of the n-SSPP estimates of $T{\rm eff}_C$, $\log g_C$, and $[{\rm Fe/H}]_C$ is on the order of 125 K, 0.5 dex, and 0.2 dex, respectively.

Figure 3 shows that a comparison with the (non-suspect) RAVE determinations is significantly worse for $T{\rm eff}_C$ but commensurate with the comparisons to the high-resolution results for $\log g_C$ and $[{\rm Fe/H}]_C$. There are too few stars in common between the stars with RAVE parameter estimates and those with high-resolution estimates to make meaningful comparisons.

Beers et al. (2014) also used literature values of [C/Fe], based on high-resolution spectroscopic analyses, to derive corrections for the n-SSPP estimates of [C/Fe], as follows:

$$[{\rm C/Fe}]_C = [{\rm C/Fe}]_S - (-0.068 \cdot [{\rm C/Fe}]_S + 0.273). \quad (4)$$

The corrected values are listed as $[{\rm C/Fe}]_C$ in column (8) of Table 3. This table also lists, in column (9), the absolute value of the carbon abundance, $A({\rm C}) = \log\epsilon\,({\rm C})$.[11] We assume, following Beers et al., that external errors for $[{\rm C/Fe}]_C$ are on the order of $\sim$0.20 dex.

The parameter CEMP, shown in column (10) of Table 3, indicates whether the star is considered carbon enhanced (CEMP = "C," satisfying $[{\rm C/Fe}]_C > +0.7$, CC $\geqslant 0.7$, and EQW $\geqslant 1.2$), of intermediate carbon enrichment (CEMP = "I," satisfying $+0.5 < [{\rm C/Fe}]_C \leqslant +0.7$, CC $\geqslant 0.7$, and EQW $\geqslant 1.2$), or carbon normal (CEMP = "N," satisfying $[{\rm C/Fe}]_C \leqslant +0.5$, CC $\geqslant +0.7$, and EQW $\geqslant 1.2$). Stars with upper limits on their carbon ratios are indicated by CEMP = "U" (these include stars with DETECT = "U," CC $\geqslant +0.7$, and DETECT = "D" but CC $< +0.7$). Stars without carbon measurements are listed as CEMP = "X." There are 48 stars listed with CEMP = "C," 29 with CEMP = "I," 1362 with CEMP = "N," and 116 with CEMP = "U."

3.4. Distance Estimates and Proper Motions

Distances to individual stars in our sample are estimated using the M_V versus $(B-V)_0$ relationships described by Beers et al. (2000). These relationships require that the likely evolutionary stage of a star be given. Assignments to the evolutionary stage, based on the derived (corrected) stellar atmospheric parameters, are as follows: dwarf, D($\log g_C \geqslant 4.0$); turnoff, TO ($3.5 \leqslant \log g_C < 4.0$); and subgiant or giant, G ($\log g_C < 3.5$). Note that refinements to this scheme, designed to resolve the possible incorrect assignments of TO stars at cooler temperatures, are adopted as described in Beers et al. (2012). Following Santucci et al. (2015), stars with effective temperature $T{\rm eff}_C \geqslant 6000$ K and $\log g_C \leqslant 3.5$ are classified as field horizontal-branch (FHB) stars.

Based on previous tests of this approach, we expect the distances assigned as described above to be accurate on the order of 15%. Fortunately, there are a small number of stars (24) in our sample with reliable distance estimates available from *Hipparcos* parallax measurements, listed in Table 4, using the van Leeuwen (2007) reduction. Column (1) lists the star names, column (2) the assigned evolutionary type, column (3) the *Hipparcos* parallax $\pi_{\rm HIP}$, column (4) the error on the parallax $\sigma_{\pi_{\rm HIP}}$, and column (5) the ratio $\sigma_{\pi_{\rm HIP}/\pi_{\rm HIP}}$. In order to be considered a reliable estimate of the parallax, this ratio should be less than 0.20. The parallax distance estimate and its error are listed as $D_{\rm HIP}$ and $\sigma_{D_{\rm HIP}}$ in columns (6) and (7), respectively. The estimated photometric distances $D_{\rm pho}$ and their errors $\sigma_{D_{\rm pho}}$ are provided in columns (8) and (9), respectively.

Figure 4 presents a comparison of the distances calculated on the basis of the photometric estimates and *Hipparcos* parallaxes. From inspection of this figure, a great majority of the stars have commensurate distance estimates; the one-sigma scatter of the residuals varies between 10% and 20%, on the order of our adopted distance error of 15%. The most deviant stars include one giant and one dwarf.

[11] A(C) is not measured directly—as it can be from high-resolution spectroscopy—but rather obtained from medium-resolution determinations using $A({\rm C}) = [{\rm C/Fe}] + [{\rm Fe/H}] + A({\rm C})_\odot$, where we adopt the solar abundance of carbon from Asplund et al. (2009), $A({\rm C})_\odot = 8.43$.

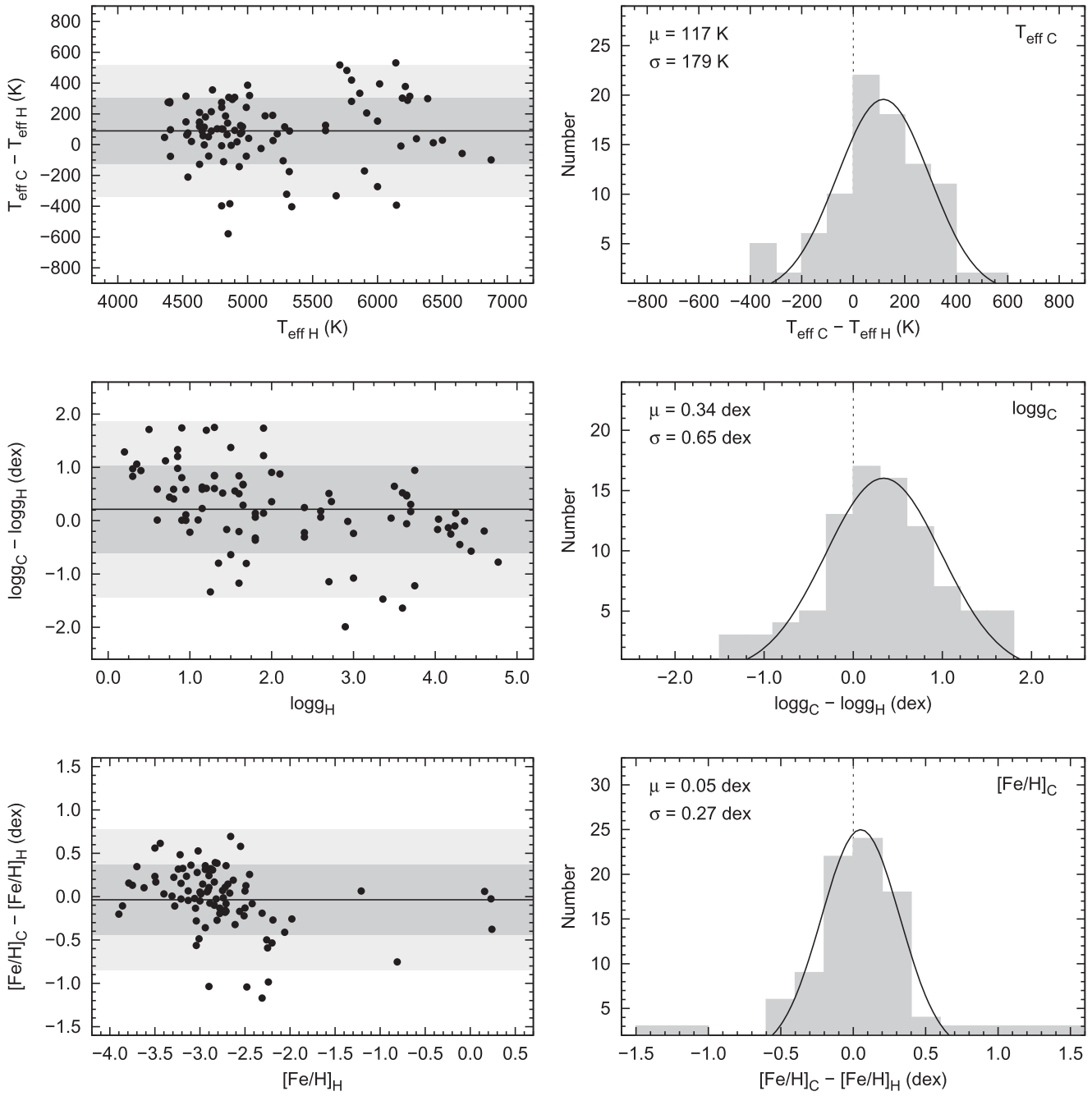

Figure 2. Left panels: differences between the (corrected) atmospheric parameters determined by the n-SSPP—$T\mathrm{eff}_C$, log g_C, and $[\mathrm{Fe/H}]_C$—and the values from analyses of high-resolution spectroscopy—$T\mathrm{eff}_H$, log g_H, and $[\mathrm{Fe/H}]_H$—reported in the literature, as a function of the high-resolution spectroscopic values. Filled symbols refer to the program stars. The horizontal solid line is the average of the residuals, while the darker and lighter shaded areas represent the 1σ and 2σ regions, respectively. Right panels: histograms of the residuals between the corrected n-SSPP and high-resolution parameters shown on the left panels. Each panel also lists the average offset and scatter determined from a Gaussian fit.

Table 5 lists star names in column (1) and the assigned type classifications, photometric distance estimates, and their errors in columns (2)–(4), respectively.

The great majority of our program stars (1732 stars) have reasonably high-quality proper motions available from the UCAC4 catalog (Zacharias et al. 2013), the SPM4 catalog (Girard et al. 2011; 321 stars), or the *Hipparcos* (van Leeuwen 2007) and Tycho II catalogs (Høg et al. 2000; 66 stars). We have chosen to adopt, where possible, the UCAC4 proper motions, since they exist for almost all of our stars and generally have very small errors. The only exception is that when proper motions are available from the *Hipparcos* or Tycho II catalogs, we adopt those. The final results are listed as μ_α and μ_δ for the proper motions in the R.A. and decl. directions, respectively, in columns (5) and (6) of Table 5. Their associated errors are listed in columns (7) and (8). The source of the adopted proper motion is listed in column (9). Note that, for a small number of stars for which some ambiguity exists as to which star of a listed pair is the one intended (generally those with "A," "B," or "F" appended to their names), we do not adopt any proper motions.

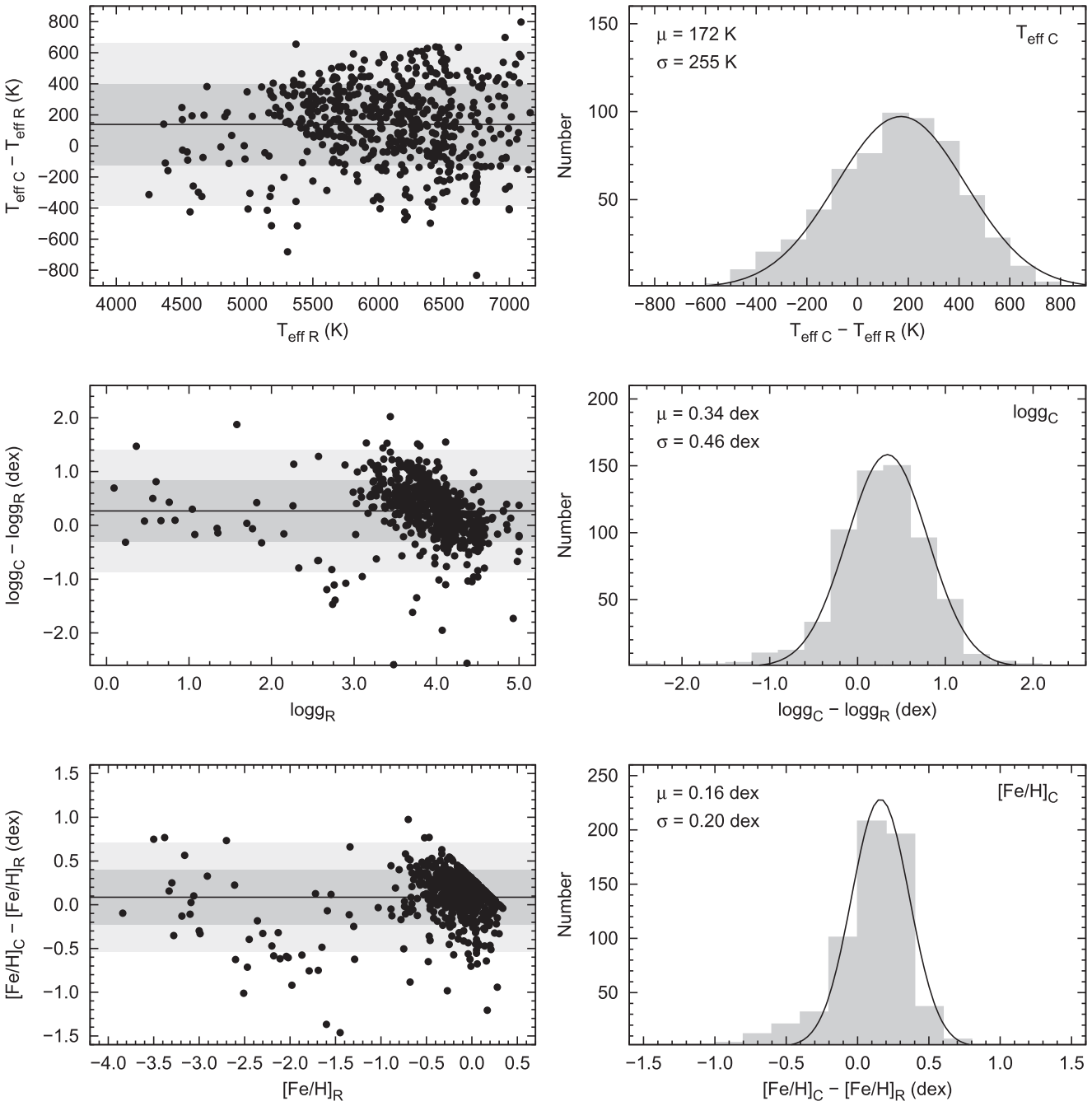

Figure 3. Left panels: Differences between the (corrected) atmospheric parameters determined by the n-SSPP—*T*eff$_C$, log g_C, and [Fe/H]$_C$—and the values from RAVE—*T*eff$_R$, log g_R, and [Fe/H]$_R$—reported in the literature, as a function of the RAVE spectroscopic values. Filled symbols refer to the program stars. The horizontal solid line is the average of the residuals, while the darker and lighter shaded areas represent the 1σ and 2σ regions, respectively. Right panels: Histograms of the residuals between the corrected n-SSPP and high-resolution parameters shown on the left panels. Each panel also lists the average offset and scatter determined from a Gaussian fit.

4. A KINEMATIC ANALYSIS OF THE COMBINED FREBEL ET AL. (2006) AND BEERS ET AL. (2014) SAMPLES

In this section we examine the kinematic properties of our program stars, in combination with a similar local sample of stars originally identified by Bidelman & MacConnell (1973) and discussed by Beers et al. (2014). The stellar parameter estimates and derived kinematic quantities of this latter sample were determined in a manner essentially identical to that for our program stars, and they supplement the numbers of stars with lower metallicity for our subsequent analysis. The corrections to the n-SSPP-derived atmospheric parameter estimates and [C/Fe] for our program stars are identical to those used by Beers et al. (2014). For simplicity, we drop the "C" subscript on the corrected stellar atmospheric parameters and the carbonicity estimates in the analysis that follows, although it is understood that these are the quantities we have adopted.

Figure 5 shows the distribution of the absorption-corrected V_0 magnitudes, de-reddened $(B-V)_0$ colors, distance estimates $D_{\rm pho}$, and estimates of metallicities [Fe/H] for our program stars from Paper I. As is immediately clear from inspection of this figure, this is a very local sample of stars,

Table 4
Parallaxes and Distance Estimates for Stars with *Hipparcos* Measurements

Star Name	Type	π_{HIP} (mas)	$\sigma_{\pi_{HIP}}$ (mas)	$\sigma_{\pi_{HIP}}/\pi_{HIP}$	D_{HIP} (kpc)	$\sigma_{D_{HIP}}$ (kpc)	D_{pho} (kpc)	$\sigma_{D_{pho}}$ (kpc)
(1)	(2)	(3)	(4)	(5)	(6)	(7)	(8)	(9)
HE 0035-0834	D	9.51	1.11	0.12	0.105	0.012	0.084	0.013
HE 0115-5135	G	6.67	1.30	0.19	0.150	0.029	0.285	0.043
HE 0134-2142	D	7.57	1.55	0.20	0.132	0.027	0.150	0.023
HE 0246-5114	D	4.31	0.66	0.15	0.232	0.036	0.199	0.030
HE 0422-4205	D	5.61	1.13	0.20	0.178	0.036	0.158	0.024
HE 0429-4149	D	13.80	0.95	0.07	0.072	0.005	0.064	0.010
HE 0435-4121	D	5.33	1.06	0.20	0.188	0.037	0.181	0.027
HE 0455-3157	D	10.05	1.31	0.13	0.100	0.013	0.076	0.011
HE 0457-3209	D	6.42	1.18	0.18	0.156	0.029	0.134	0.020
HE 0511-4835	D	11.23	0.92	0.08	0.089	0.007	0.099	0.015
HE 0520-5617	D	4.55	0.50	0.11	0.220	0.024	0.142	0.021
HE 1108-3217	D	6.80	0.60	0.09	0.147	0.013	0.049	0.007
HE 1120-0858	D	8.32	1.49	0.18	0.120	0.022	0.177	0.027
HE 1211-3038	D	13.81	1.50	0.11	0.072	0.008	0.100	0.015
HE 1223-0133	TO	9.05	1.11	0.12	0.110	0.014	0.125	0.019
HE 1349-1827	FHB	4.57	0.76	0.17	0.219	0.036	...	...
HE 1411-0542	TO	23.33	0.53	0.02	0.043	0.001	0.022	0.003
HE 1450-1808	D	25.31	1.85	0.07	0.040	0.003	0.027	0.004
HE 2231-0149	D	9.38	0.47	0.05	0.107	0.005	0.283	0.042
HE 2255-1758	D	5.14	0.88	0.17	0.195	0.033	0.175	0.026
HE 2307-4543	D	22.13	1.31	0.06	0.045	0.003	0.046	0.007
HE 2327-4203	D	10.17	1.19	0.12	0.098	0.012	0.145	0.022
HE 2332-4431	D	10.06	1.78	0.18	0.099	0.018	0.127	0.019
HE 2333-4047	D	8.67	1.65	0.19	0.115	0.022	0.110	0.017
HE 2333-4325	TO	6.47	1.31	0.20	0.155	0.031	0.149	0.022

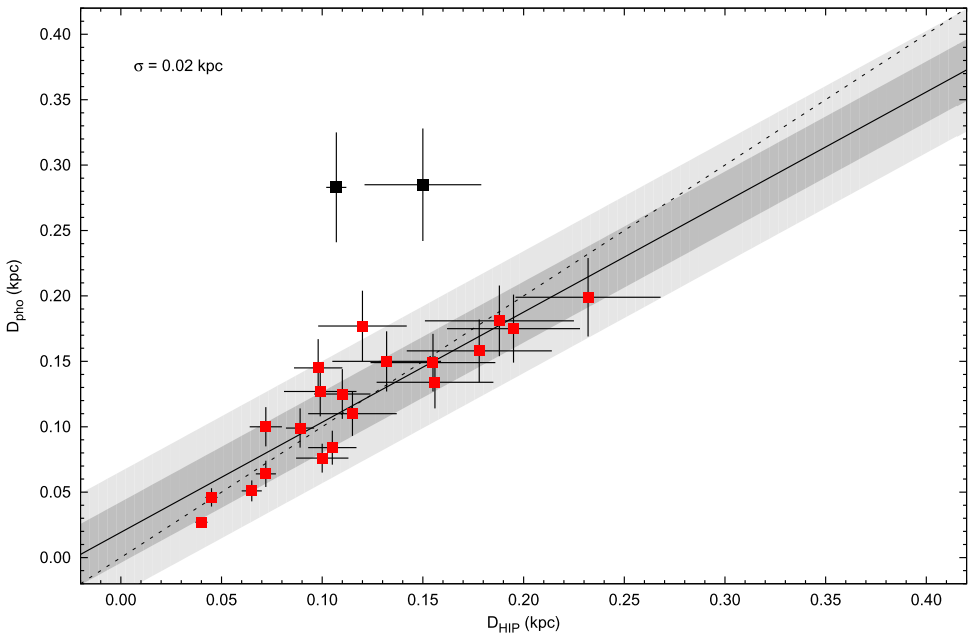

Figure 4. Comparison of the photometrically estimated distances D_{pho} with the trigonometric distance estimates D_{HIP} for stars with sufficiently accurate *Hipparcos* parallaxes ($\sigma_{\pi_{HIP}}/\pi_{HIP} \leqslant 0.20$). The dashed line is the one-to-one line, while the solid line is a robust regression fit to the data. The darker and lighter shaded areas represent the 1σ and 2σ regions about the linear fit, respectively, based on a Gaussian fit to the residuals. The most deviant stars include one giant and one dwarf.

$\sim$90% of which are located within 0.5 kpc of the Sun. Although the majority of the sample stars have metallicities close to Solar, some 20% (351 stars) of the stars with available metallicity estimates have [Fe/H] $\leqslant -0.5$, 14% (248 stars) have [Fe/H] $\leqslant -1.0$, 12% (213 stars) have [Fe/H] $\leqslant -1.5$, and 10% (171 stars) have [Fe/H] $\leqslant -2.0$. Figure 6 of Beers et al. (2014) shows similar information for that sample. As can be appreciated from inspection of that figure, these stars include a larger fraction of giants, which explore slightly farther from the Sun, up to 2 kpc (although $\sim$90% are within 1 kpc of the Sun). Unlike the Paper I stars, almost half of the supplemental sample (145 stars) have [Fe/H] $\leqslant -1.0$; there are also 36 stars with [Fe/H] $\leqslant -2.0$, which makes them useful for our exploration of metal-poor populations of the Galaxy.

Table 5
Distance Estimates and Proper Motions

Star Name	Type	D_{pho} (kpc)	$\sigma_{D_{pho}}$ (kpc)	μ_α (mas yr^{-1})	μ_δ (mas yr^{-1})	σ_{μ_α} (mas yr^{-1})	σ_{μ_δ} (mas yr^{-1})	PM Source
(1)	(2)	(3)	(4)	(5)	(6)	(7)	(8)	(9)
HE 0000-3017	D	0.249	0.037	20.0	1.3	1.1	0.8	U
HE 0000-4401	D	0.174	0.026	23.6	11.5	1.0	2.9	U
HE 0000-5703	D	0.253	0.038	13.9	2.6	0.9	1.0	U
HE 0001-4157	D	0.107	0.016	−19.9	−54.8	0.8	0.8	U
HE 0001-4449	TO	0.223	0.033	−1.0	0.7	1.1	1.0	U
HE 0001-5640	D	0.249	0.037	40.2	−13.0	1.0	1.2	U
HE 0002-3233	TO	0.430	0.065	57.4	−31.6	1.3	1.5	U
HE 0002-3822	D	0.158	0.024	−36.2	−8.9	1.0	1.5	U
HE 0002-5625	D	0.258	0.039	11.8	−4.9	1.4	1.4	U
HE 0003-0503	G	0.163	0.024	9.5	−1.5	1.8	1.3	U

Note. Sources of proper motions: U = UCAC4, S = SPM4, H = *Hipparcos* or Tycho II.
(This table is available in its entirety in machine-readable form.)

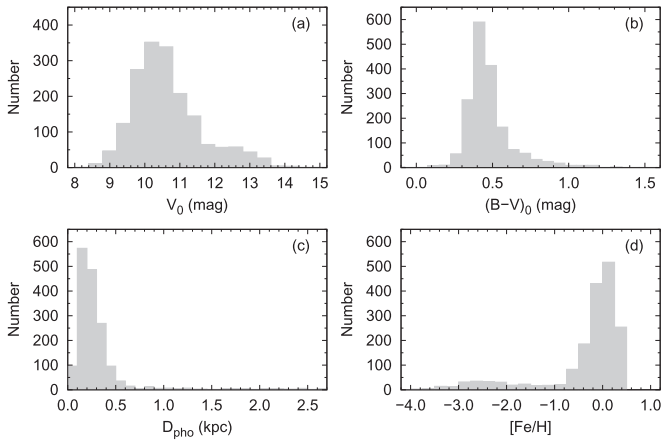

Figure 5. Distributions of (a) absorption-corrected V_0 magnitudes, (b) de-reddened $(B-V)_0$ colors, (c) photometric distance estimates D_{pho}, and (d) metallicity estimates [Fe/H] for our program stars.

4.1. Determination of U, V, and W Velocity Components and Orbital Eccentricities for the Frebel et al. (2006) Sample

The derivation of space motions and orbital parameters of our program stars from Paper I follows the procedures described by Carollo et al. (2010), which for convenience are summarized below. Similar procedures were employed by Beers et al. (2014) for the supplemental stars; results are listed in Table 5 of that paper.

Corrections for solar motion with respect to the local standard of rest (LSR) are applied during the course of the calculation of the full space motions; here we adopt the values $(U, V, W) = (9, 12, 7)$ km s^{-1} (Mihalas & Binney 1981). We follow the convention that U is positive in the direction away from the Galactic center, V is positive in the direction of Galactic rotation, and W is positive toward the north Galactic pole. It is also convenient to obtain the rotational component of a star's motion about the Galactic center in a cylindrical frame, denoted as V_ϕ and calculated assuming that the LSR is in a circular orbit with a value of 220 km s^{-1} (Kerr & Lynden-Bell 1986). Our assumed values of the solar radius ($R_\odot = 8.5$ kpc) and the circular velocity of the LSR are both consistent with two recent independent determinations of these quantities by Ghez et al. (2008) and Koposov et al. (2009). Bovy et al. (2012) obtained an estimate of the Milky Way's circular velocity at the position of the Sun of $V_c(R_\odot) = 218 \pm 6$ km s^{-1}, based on an analysis of high-resolution spectroscopic determinations from APOGEE, which is also consistent with our adopted value.

The orbital parameters of the stars, including the perigalactic distance r_{peri}(the closest approach of an orbit to the Galactic center), the apogalactic distance r_{apo} of each stellar orbit (the farthest extent of an orbit from the Galactic center), and the orbital eccentricity $e = (r_{apo} - r_{peri})/(r_{apo} + r_{peri})$, as well as Z_{max} (the maximum distance that a stellar orbit achieves above or below the Galactic plane), are derived by adopting an analytic Stäckel-type gravitational potential (which consists of a flattened, oblate disk and a nearly spherical massive dark-matter halo; see the description given by Chiba & Beers 2000, Appendix A) and integrating their orbital paths based on the starting point obtained from the observations.

Table 6 provides a summary of the above calculations. Column (1) provides the star names. Columns (2) and (3) list the positions of the stars in the meridional (R, Z)-plane. The derived U, V, and W velocity components are provided in columns (4)–(6); their associated errors are listed in columns (7)–(9). Column (10) lists the velocity projected onto the Galactic plane (V_R, positive in the direction away from the Galactic center), while column (11) lists the derived rotation velocity V_ϕ. The derived r_{peri} and r_{apo} are given in columns (12) and (13), respectively. Columns (14) and (15) list the derived Z_{max} and orbital eccentricity e, respectively. The INOUT parameter listed in column (16) is set to 1 if the star is considered in our kinematic analysis, and set to 0 if not.

Errors on our derived estimates of the individual components of the space motions take into account an estimated 15% error in the photometric distances, as well as the individual errors in the proper motions (the average error on our adopted proper motions is 1.3 mas yr^{-1} in each of the R.A. and decl. component directions) and in the adopted radial velocities (2 km s^{-1} for the high-resolution determinations, 5 km s^{-1} for the moderate-resolution determinations, and 10 km s^{-1} for the medium-resolution determinations). Figure 6 shows the distributions of these errors. After removing the 145 stars that are missing one or more of the input quantities used for the determination of their space motions or have individual estimated errors larger than 50 km s^{-1} in any one of the three components of space motion, we obtain for our program sample average errors of $\sigma(U, V, W) = (5.9, 6.3, 6.9)$ km s^{-1}.

Table 6
Space Motions and Orbital Parameters

Star Name	R (kpc)	Z (kpc)	U (km s^{-1})	V (km s^{-1})	W (km s^{-1})	$\sigma(U)$ (km s^{-1})	$\sigma(V)$ (km s^{-1})	$\sigma(W)$ (km s^{-1})	V_R (km s^{-1})	V_ϕ (km s^{-1})	r_{peri} (kpc)	r_{apo} (kpc)	Z_{max} (kpc)	e	INOUT
(1)	(2)	(3)	(4)	(5)	(6)	(7)	(8)	(9)	(10)	(11)	(12)	(13)	(14)	(15)	(16)
HE 0000-3017	8.454	−0.244	8	4	−19	4	2	10	9	224	8.30	8.82	0.36	0.03	1
HE 0000-4401	8.450	−0.164	12	12	3	4	2	5	12	232	8.34	9.32	0.18	0.06	1
HE 0000-5703	8.407	−0.217	−3	−2	−20	3	2	4	−6	218	8.10	8.47	0.34	0.02	1
HE 0001-4157	8.471	−0.102	−26	−6	26	3	3	5	−27	213	7.50	8.99	0.35	0.09	1
HE 0001-4449	8.436	−0.210	−7	15	16	2	1	5	−8	235	8.39	9.51	0.32	0.06	1
HE 0001-5640	8.410	−0.215	32	−17	18	7	6	9	30	203	6.90	8.81	0.33	0.12	1
HE 0002-3233	8.417	−0.422	52	−98	−68	12	17	10	52	122	3.54	8.84	1.61	0.43	1
HE 0002-3822	8.462	−0.153	−34	19	21	5	2	10	−34	239	8.04	10.45	0.35	0.13	1
HE 0002-5625	8.407	−0.223	−6	−7	−12	4	4	9	−9	213	7.72	8.48	0.27	0.05	1
HE 0003-0503	8.506	−0.148	−2	22	−26	2	2	5	0	242	8.51	10.19	0.43	0.09	1

Note. INOUT takes on a value of "1" if the star is accepted for the kinematic analysis, or "0" if not.

(This table is available in its entirety in machine-readable form.)

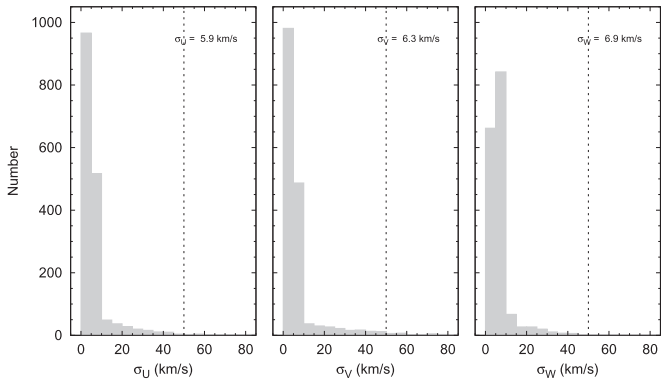

Figure 6. Errors in the estimation of the local velocity components of the space motions for the Paper I stars. The vertical dashed lines at 50 km s^{-1} indicate the maximum individual errors allowed for a given star to be included in the subsequent kinematic analysis. The legends provide the mean errors for the accepted stars.

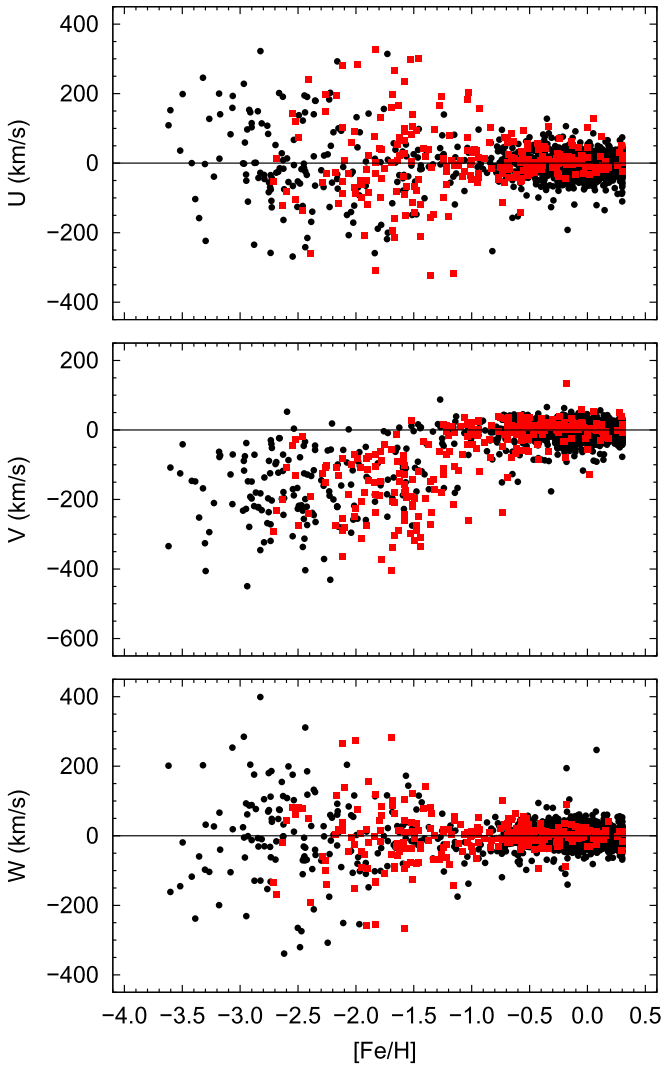

Figure 7. Local velocity components for the combined sample of Paper I stars (shown as black dots) and the supplemental stars from Beers et al. (2014) (shown as red squares) with available *UVW* estimates, as a function of metallicity [Fe/H]. Note the existence of stars with low velocity dispersions in their estimated components down to at least [Fe/H] = −1.3 (possibly a little lower). Stars with errors exceeding 50 km s^{-1} in any of the individual derived components of motion are excluded.

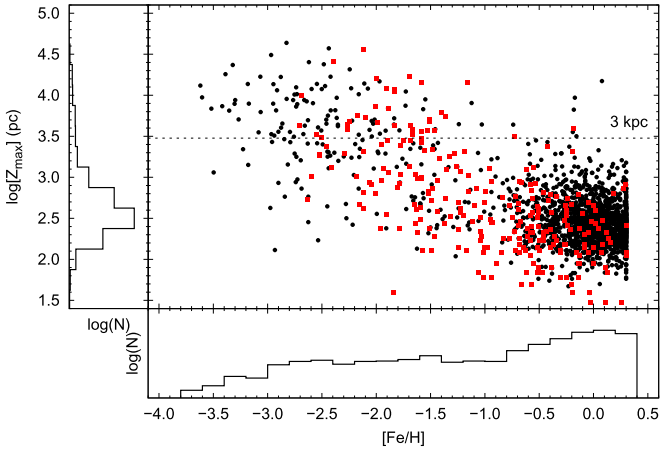

Figure 8. Distribution of $Z_{\rm max}$, the largest distance above or below the Galactic plane achieved by a star during the course of its orbit, as a function of metallicity [Fe/H] for the combined sample of Paper I stars (shown as black dots) and supplemental stars from Beers et al. (2014; shown as red squares). The marginal distributions of each variable are shown as histograms. The horizontal dashed line provides a reference at 3 kpc. Very few stars with metallicity [Fe/H] > -1.5 achieve orbits that reach higher than this location. Note the logarithmic scale for $Z_{\rm max}$. Stars with errors exceeding 50 km s^{-1} in any of the individual derived components of motion are excluded.

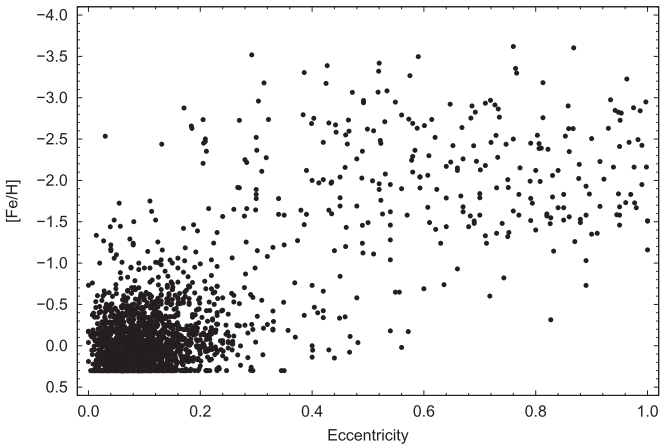

Figure 9. Distribution of metallicity [Fe/H] for the combined sample of stars as a function of derived orbital eccentricity. Stars with errors exceeding 50 km s^{-1} in any of the individual derived components of motion are excluded.

These are slightly smaller errors than were acquired (after the removal of stars having errors in U, V, or W greater than 50 km s^{-1}) for the supplemental stars from Beers et al. (2014), who reported $\sigma\,(U,\,V,\,W) = (7.9, 9.1, 6.5)$ km s^{-1}, presumably due to the inclusion of more distant stars with less certain distances and proper motions.

For the remaining analysis, we combine our program stars from Paper I with the supplemental sample based on the Beers et al. (2014) analysis of the "weak metal" stars from Bidelman & MacConnell (1973). For the purpose of the kinematic analysis, both samples have had stars with errors in excess of 50 km s^{-1} in any of the U, V, W velocity components removed from consideration.

4.2. Distributions of U, V, W, and $Z_{\rm max}$ versus [Fe/H]

Figure 7 presents the individual components of the space motions as a function of [Fe/H] for our combined sample with accepted kinematic estimates; the program stars from Paper I are shown as black dots, while the supplemental

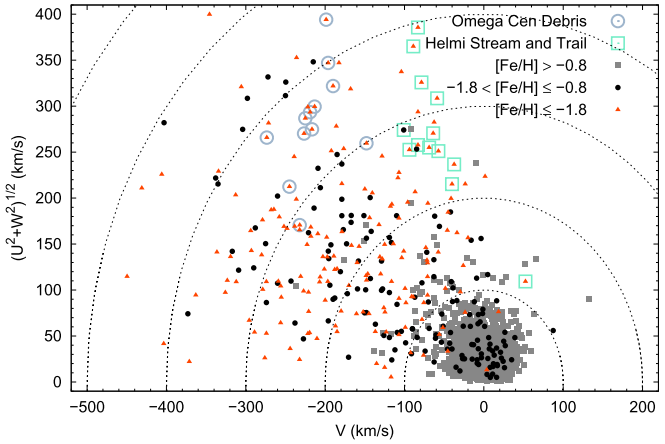

Figure 10. Toomre diagram of $(U^2 + W^2)^{1/2}$ vs. V for stars in the combined sample with available UVW velocity components, in three regimes of metallicity as indicated in the legend. The legend also indicates the color/symbol coding used to indicate likely members of stars in the debris stream associated with the globular cluster ω Cen (light-blue circles) and the Helmi et al. stream/trail (light-green squares). See text for more details. Note the presence of intermediate-metallicity ($-1.8 < [Fe/H] \leqslant -0.8$) stars both inside and outside the region with low $(U^2 + W^2)^{1/2}$ and high orbital rotation velocities ($(U^2 + W^2)^{1/2} \lesssim 100$ km s^{-1}, $-100 < V < 100$ km s^{-1}). Stars with errors exceeding 50 km s^{-1} in any of the individual derived components of motion are excluded.

sample stars are indicated as red squares. From inspection of this figure, the two samples cover similar ranges of [Fe/H], although in different proportions—the Paper I sample dominates above [Fe/H] $= -1.0$, the supplemental sample stars exceed the Paper I stars in the metallicity interval $-2.0 <$ [Fe/H] < -1.0 by about a factor of two, and the Paper I stars dominate the combined sample of stars with [Fe/H] < -2.0, in particular for [Fe/H] < -3.0. The combined sample is heavily populated by stars in the thin-disk and thick-disk stellar populations. Some low-metallicity stars with V velocities in the interval -40 to -80 km s^{-1} are also present and are likely to be associated with the MWTD.

Figure 8 is a plot of Z_{max} as a function of [Fe/H] for the combined sample of stars. From inspection of this figure, it is clear that both the Paper I and supplemental samples explore similar regions of this space, further justifying a joint kinematic analysis. For the remainder of our analysis, we thus choose to suppress identification of the individual samples.

As seen in Figure 8, only a handful of stars with metallicities above [Fe/H] $= -1.5$ are found to have $Z_{max} > 3$ kpc. Following previous results from, e.g., Carollo et al. (2010), stars with $Z_{max} \leqslant 3$ kpc and $-1.8 \leqslant$ [Fe/H] $\leqslant -0.8$ are likely to be associated with the MWTD, although some overlap with the inner-halo population is not precluded, especially at the low end of this metallicity range. Further interpretation of the nature of the MWTD as an individual component is limited by the relatively small numbers of stars, even in the combined sample, that are available in the pertinent metallicity interval.

4.3. The [Fe/H] versus Eccentricity Diagram

Figure 9 shows a plot of [Fe/H] as a function of orbital eccentricity for the combined sample of stars. As seen previously (e.g., Norris et al. 1985; Chiba & Beers 2000; Carollo et al. 2007, 2010; Beers et al. 2014), the orbital eccentricity for these *non-kinematically selected* stars exhibits a very broad metallicity distribution, outside of the region of the metal-richest stars with $e \leqslant 0.2$–0.3, as expected from the currently favored hierarchical assembly model for the formation of the Milky Way.

4.4. The Toomre Diagram, the Distribution of V_ϕ, Integrals of Motion, and the Lindblad Diagram

The so-called Toomre diagram (a plot of $(U^2 + W^2)^{1/2}$, the quadratic addition of the U and W velocity components as a function of the rotational component V), the distribution of orbital rotation velocity V_ϕ for cuts in orbital eccentricity and [Fe/H], plots of the perpendicular angular momentum component $L_\perp$ as a function of the vertical angular momentum component L_Z, and the Lindblad diagram (a plot of the integral of motion representing the total energy E as a function of L_Z) are commonly used to investigate the nature of the kinematics of stellar populations in the Galaxy. Given the high quality of the estimated kinematics for our combined sample of stars, it is worthwhile to investigate what can be learned from inspection of these diagrams, as discussed individually below.

4.4.1. The Toomre Diagram

Figure 10 shows the Toomre diagram for the combined sample of stars; the legend indicates the metallicity intervals chosen to roughly separate stars expected to belong to the thick (or thin) disk ([Fe/H] > -0.8), the MWTD ($-1.8 <$ [Fe/H] $\leqslant -0.8$), and the halo system ([Fe/H] $\leqslant -1.8$) in accordance with Carollo et al. (2010). As expected, the more metal-rich stars in both samples are primarily found in the region with low $(U^2 + W^2)^{1/2}$ and high orbital rotation velocities, $(U^2 + W^2)^{1/2} \lesssim 100$ km s^{-1} and $-100 < V < 50$ km s^{-1}, while stars with intermediate metallicities are divided between those inside and outside this region. We expect that many of the intermediate-metallicity stars inside this region are associated with the MWTD component. It is also clear from inspection of this figure that the lowest-metallicity stars, with [Fe/H] $\leqslant -1.8$, are the dominant contributors to the distribution of stars in the higher-energy regions (those beyond the circle that intersects $V = -300$ km s^{-1}), as might be expected if they are primarily comprised of members of the outer-halo population, with some overlap from members of the inner-halo population. The stars with energies that place them between the $V = -300$ km s^{-1} and $V = -200$ km s^{-1} surfaces exhibit a broader range of metallicity, as expected from overlapping inner- and outer-halo populations.

Figure 10 also indicates two subsets of (newly identified) stars in the combined sample that may belong to previously identified structures in phase-space: (1) likely members of the stream/trail of stars first identified by Helmi et al. (1999) and further populated by stars in the sample considered by Chiba & Beers (2000), indicated by light-green squares, and (2) possible members of the debris stream associated with the globular cluster ω Cen, following the work of Dinescu (2002), Klement et al. (2009), and Majewski et al. (2012), indicated by light-blue circles. Justification for the selection of these stars is provided below.

4.4.2. Distribution of V_ϕ

Figure 11 is a stripe-density diagram of the distribution of V_ϕ for our combined sample of stars for metallicity intervals chosen to emphasize the various kinematic components of the Milky Way, split into two regions of orbital eccentricity, $e \leqslant 0.3$ (upper panels, expected to be dominated by members

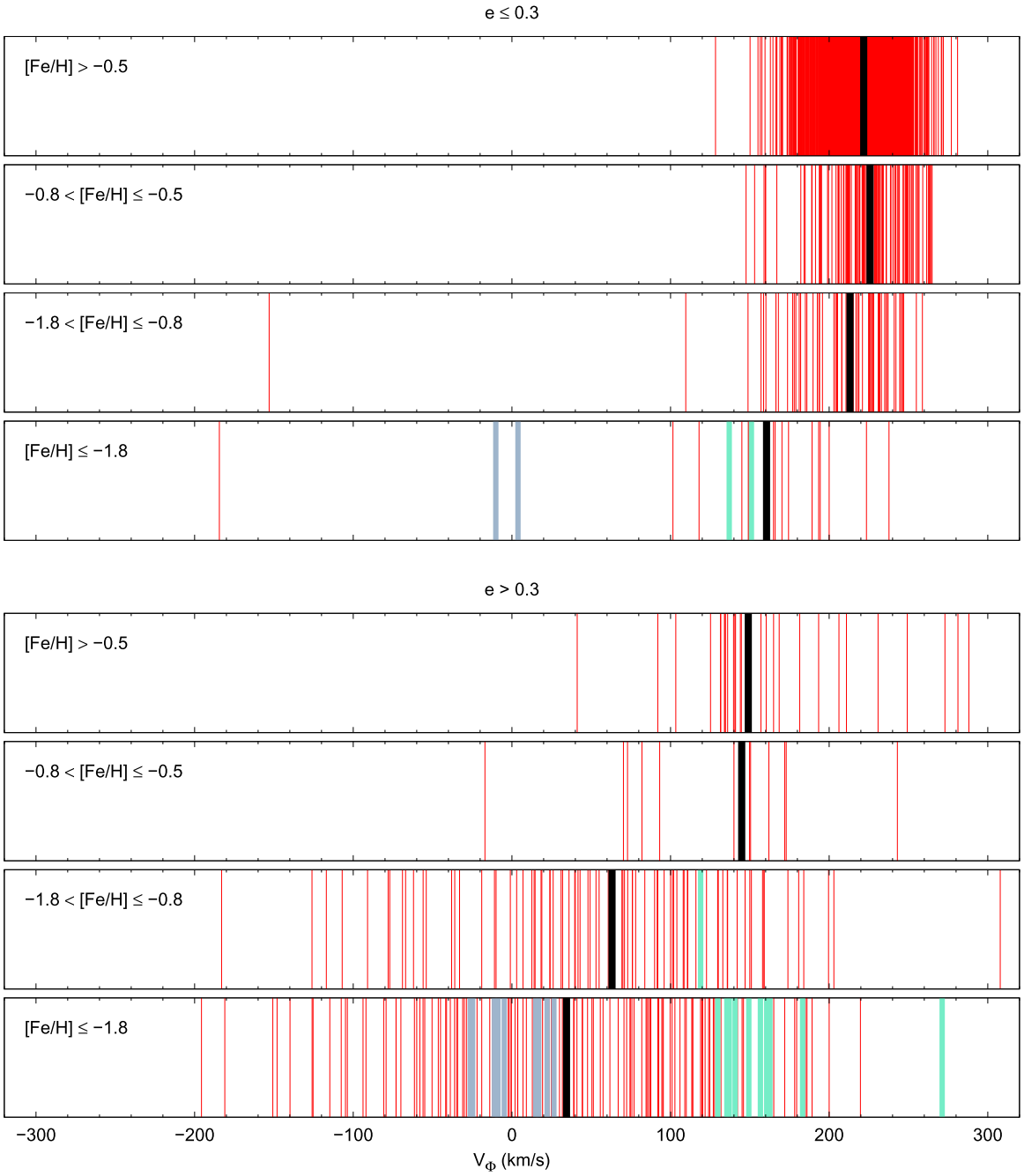

Figure 11. Stripe-density diagrams of the rotational velocity V_ϕ for stars in the combined sample. The plots are split into low-eccentricity ($e \leqslant 0.3$; upper panels) and high-eccentricity ($e > 0.3$; lower panels) sub-samples. Each sub-sample is further divided into metallicity intervals chosen to separate regions dominated by individual components of the disk and halo systems. See text for more details. The black stripes indicate the mean V_ϕ for the stars in each subset. The light-blue and light-green stripes indicate stars identified as likely members of stars in the debris stream associated with the globular cluster ω Cen and the Helmi et al. stream/trail, respectively. Stars with errors exceeding 50 km s^{-1} in any of the individual derived components of motion are excluded.

of the disk system) and $e > 0.3$ (lower panels, expected to be dominated by members of the halo system). For each interval in metallicity, the black stripes indicate the mean V_ϕ for that sub-sample of stars. The light-green and light-blue stripes indicate stars that we argue below are candidate members of the Helmi et al. stream/trail and the ω Cen debris streams, respectively.

Inspection of Figure 11 generally meets expectation based on previous work. The low-eccentricity stars for all three sub-panels with [Fe/H] > -1.8 exhibit rotational properties consistent with those of the disk system of the Milky Way (thin disk, thick disk, and MWTD), while those with [Fe/H] $\leqslant -1.8$ appear to be primarily members of the inner- and outer-halo populations. The high-eccentricity stars preferentially populate the sub-panels with $-1.8 <$ [Fe/H] $\leqslant -0.8$ and [Fe/H] $\leqslant -1.8$, consistent with membership in the inner- and outer-halo populations, with overlapping contributions from each.

It is worth noting that the presence of putative members of the two debris streams has a potentially large impact on interpretation of the distribution of V_ϕ among the high-eccentricity stars with [Fe/H] < -1.8, with these members populating both the central region of the stripe plot (the Helmi

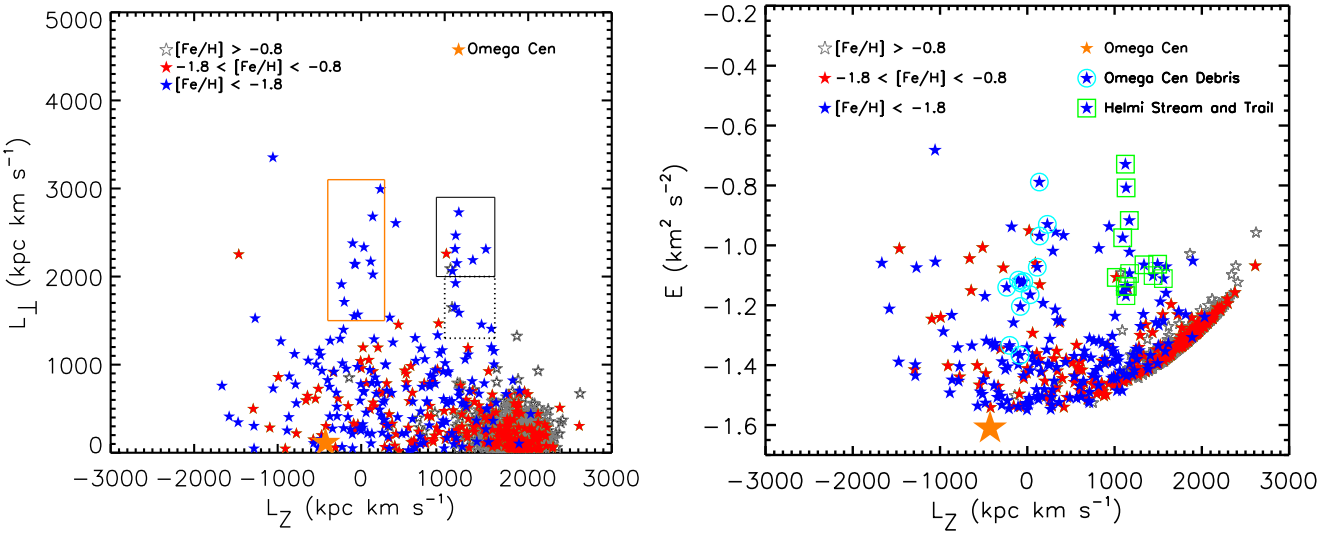

Figure 12. Left panel: distribution of the angular momentum components $L_\perp$ and L_Z for the combined sample of stars over three ranges of metallicity, as shown in the legend. The solid and dotted black boxes denote the region of the clumps that are likely associated with the Helmi et al. stream and trail, respectively. The orange box represents the region of the putative debris stream associated with the ω Cen globular cluster. The position of this cluster in this diagram is indicated by the large orange star. Stars with errors exceeding 50 km s^{-1} in any of the individual derived components of motion are excluded. Right panel: Lindblad diagram of the distribution of the total energy E (in units of 10^5) as a function of the vertical angular momentum L_Z over three ranges of metallicity, as shown in the legend. Likely members of the Helmi et al. stream and its trail are highlighted with light-blue circles; stars that are likely members of the putative ω Cen debris stream are indicated by light-green squares. The position of this cluster in this diagram is indicated by the large orange star. Stars with errors exceeding 50 km s^{-1} in any of the individual derived components of motion are excluded.

et al. stream/trail) and the high-velocity tail (the ω Cen debris stream).

4.4.3. $L_\perp$ versus L_Z

The left panel of Figure 12 shows the distribution of stars in angular momentum space ($L_\perp$, L_Z), where $L_\perp = (L_X^2 + L_Y^2)$ and L_Z is the vertical angular momentum. The three different ranges of metallicity are identified with different colors, shown in the figure legend.

Two interesting features are seen in this diagram: (1) a clump of stars with [Fe/H] < -1.8 (with the exception of two stars with higher metallicity) located at $L_\perp \sim 2000$–2900 kpc km s^{-1} and $L_Z \sim 800$–1600 kpc km s^{-1} (indicated by the solid black box in the figure) and (2) an elongated distribution of stars with [Fe/H] $\leqslant -1.8$ located at $L_\perp > 1500$ km s^{-1} and $-400 \lesssim L_Z \lesssim 300$ kpc km s^{-1} (indicated by the orange box).

The first feature was identified by Helmi et al. (1999), comprising 7 stars with [Fe/H] $\leqslant -1.6$ and 12 stars with [Fe/H] $\leqslant -1.0$. Chiba & Beers (2000) detected the same stream among their sample of 1203 stars over similar ranges in metallicity. They also identified a possible trail in angular momentum space located at 1250 kpc km s^{-1} $< L_\perp <$ 2000 kpc km s^{-1} and 1200 kpc km s^{-1} $< L_Z <$ 2000 kpc km s^{-1} and covering similar metallicity ranges (their Figure 15). This is similar to the trail identified in Figure 12, occupying the region defined by the dotted black box and covering angular momentum ranges of $L_\perp = [1300, 2000]$ kpc km s^{-1} and $L_Z = [1000, 1600]$ kpc km s^{-1}, but at lower metallicities [Fe/H] $\leqslant -1.8$. Note that a few stars with metallicities above [Fe/H] $= -1.8$ are also within the areas delimited by the two boxes associated with the Helmi et al. stream/trail.

The second feature (orange box) is similar to the excess of stars located in the phase-space noted by Dinescu (2002) within the Chiba & Beers (2000) data set. Dinescu argued that these stars may be part of a debris stream associated with the globular cluster ω Cen. Dinescu (2002) found that most of the stars in this region possessed slightly retrograde orbits, as is also the case for ω Cen, and discovered another two clusters (NGC 362 and NGC 6779) that present similar retrograde orbits. The author also suggested that the cluster ω Cen (shown as a large orange star in the figure), as well as the two other globular clusters, may have been stripped, along with numerous other stars, from a proposed parent dwarf galaxy now dissolved into the halo-system population.

4.4.4. The Lindblad Diagram, E versus L_Z

The right panel of Figure 12 is the so-called Lindblad diagram for the combined sample, split into the same metallicity ranges as on the left panel. Stars associated with the Helmi et al. (1999) stream and its trail are indicated with light-green boxes around them, while those identified as possible members of the ω Cen debris stream are indicated with light-blue circles around them. The Helmi et al. stream and its trail occupy a range of orbital energy $E = [-1.2, -0.7]$ km^2 s^2 (in units of 10^5), while the putative ω Cen stellar debris stream stars have orbital energies spanning E: $[-1.35, -0.8]$ km^2 s^2.

The stars we identify as members of these structures are listed in column (1) of Table 7, along with their coordinates (column 2), photometry (columns 3 and 4), derived metallicity [Fe/H] (column 5), carbonicity [C/Fe] (column 6), and absolute carbon abundance A(C) (column 7), as well as their integrals of motion (columns 9–11). We have verified that these stars are not among those previously identified by Chiba & Beers (2000). There are five CEMP stars among the proposed ω Cen debris stream listed in this table, with carbonicities in the range [C/Fe] $= [+0.73, +1.47]$. The listed absolute carbon abundances for four of these stars, A(C), are all below 7.1; according to the Yoon–Beers diagram of A(C) versus [Fe/H] (Yoon et al. 2016; Figure 1), they would be classified as CEMP-no stars. There is one star in the proposed ω Cen debris

Table 7
Parameters for Stars in the Identified Streams

Star Name	R.A. (2000) Decl.	V (mag)	$B-V$ (mag)	$[Fe/H]_C$	$[C/Fe]_C$	A(C)	Class	$L_\perp$ (kpc km s^{-1})	L_Z (kpc km s^{-1})	E (10^5 km^2 s^{-2})
(1)	(2)	(3)	(4)	(5)	(6)	(7)	(8)	(9)	(10)	(11)
Helmi et al. Debris Stream										
HE 0012-5643[a]	00 15 17.1 −56 26 27	12.29	0.46	−2.97	+1.41	6.87	CEMP-*s*	2466	1132	−0.81
HE 0017-3646	00 20 26.1 −36 30 20	13.02	0.54	−2.48	−0.54	5.41	...	2729	1169	−0.92
HE 0048-1109[a]	00 51 26.4 −10 53 14	10.83	0.49	−1.97	−0.10	6.36	...	2187	1337	−1.07
BM-028	02 47 37.4 −36 06 27	9.94	0.46	−1.58	+0.24	7.31	...	2259	1020	−1.11
HE 0324-0122	03 27 02.3 +01 32 33	12.13	0.72	−2.11	+0.37	6.69	...	2311	1493	−1.06
BM-209	14 36 48.5 −29 06 47	8.02	0.64	−1.91	+0.06	6.66	...	2152	1146	−1.14
HE 2215-3842	22 18 20.9 −38 27 55	13.40	0.68	−2.24	+0.45	6.64	...	2062	1093	−0.97
BM-308	22 37 08.1 −40 30 39	9.11	0.79	−2.12	−0.10	6.39	...	2313	1124	−0.73
Helmi et al. Trail										
HE 0033-2141[a]	00 35 42.1 −21 24 58	12.29	0.72	−2.73	+0.15	5.85	...	1407	1559	−1.11
HE 0050-0918	00 52 41.7 −09 02 23	11.06	0.71	−2.08	−0.26	6.09	...	1653	1122	−1.14
HE 1210-2729[a]	12 13 07.9 −27 45 50	12.54	0.86	−2.95	−0.18	5.31	...	1589	1172	−1.09
BM-235	17 52 35.9 −69 01 45	9.48	1.05	−1.83	−0.44	6.39	...	1925	1130	−1.17
HE 2234-4757[a]	22 37 20.4 −47 41 38	12.39	0.92	−2.59	−0.26	5.57	...	1455	1441	−1.10
ω Cen Debris Stream										
HE 0007-1752[a]	00 10 17.6 −17 35 38	11.54	0.65	−2.47	+0.54	6.50	...	2333	33	−1.17
HE 0039-0216[a]	00 41 53.6 −02 00 33	13.35	0.37	−2.62	+1.40	7.21	CEMP-*s*	2993	230	−0.93
HE 0429-4620	04 30 48.6 −46 13 53	13.10	0.62	−2.42	+0.58	6.59	...	1912	−236	−1.14
HE 1120-0153[a]	04 38 55.7 −13 20 48	11.68	0.44	−2.39	−0.17	5.89	...	2023	140	−0.97
BM-056	05 10 49.6 −37 49 03	9.50	0.86	−2.00	−0.16	7.62	...	2377	−102	−1.12
BM-121[a]	09 53 39.2 −22 50 08	9.39	1.16	−2.69	−0.53	5.65	...	1550	−84	−1.37
HE 1120-0153[a]	11 22 43.2 −02 09 36	11.68	0.44	−2.88	+1.09	6.64	CEMP-no	1569	−41	−1.12
HE 1401-0010[a]	14 04 03.4 −00 24 25	13.51	0.41	−2.44	+0.73	6.72	CEMP-no	2681	138	−0.79
HE 2138-0314[a]	21 40 41.5 −03 01 17	13.23	0.57	−3.07	+0.90	6.27	CEMP-no	2138	−70	−1.13
HE 2315-4306	23 18 19.0 −42 50 27	11.28	0.65	−2.36	+0.37	6.43	...	1712	−202	−1.33
HE 2319-5228[a]	23 21 58.1 −52 11 43	13.25	0.90	−3.39	+1.47	6.51	CEMP-no	2170	114	−1.07
HE 2322-6125[a]	23 25 34.6 −61 09 10	12.47	0.63	−2.50	+0.17	6.10	...	2145	−80	−1.20

Note.
[a] A high-resolution spectrum exists for this star.

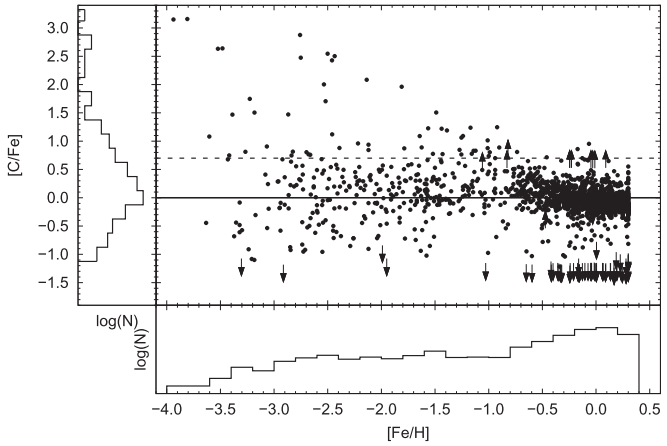

Figure 13. Carbonicity [C/Fe] as a function of metallicity [Fe/H] for the combined sample of stars with available measurements. Downward arrows indicate the derived upper limits for [C/Fe], and upward arrows indicate the lower limits. The marginal distributions of each variable are shown as histograms. The horizontal dashed line marks the level of carbon enhancement used in this paper to indicate CEMP stars, [C/Fe] $> +0.7$.

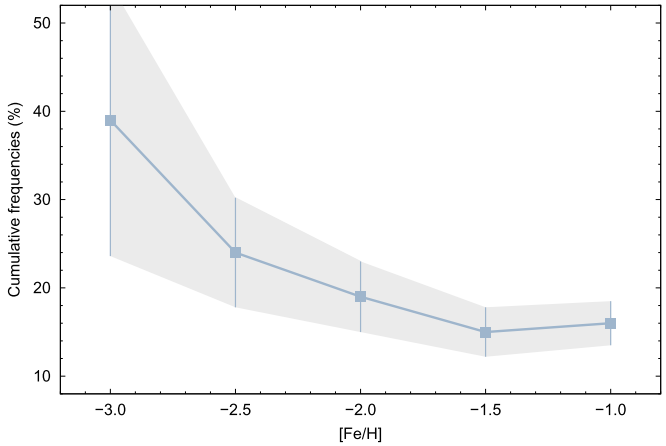

Figure 14. Cumulative frequencies of CEMP stars as a function of metallicity [Fe/H] for stars in the combined sample with available measurements. A total of 328 stars with [Fe/H] < -1.0 are included in this diagram, 52 of which are considered CEMP stars, with [C/Fe] $> +0.7$. The error bars shown are based on Poisson statistics.

stream with A(C) > 7.1, which would suggest its identification as a CEMP-*s* star. The CEMP sub-classifications are shown in column (8) of Table 7.

In a previous study, Majewski et al. (2012) identified a number of carbon-enhanced stars from the Grid Giant Stream Survey sample that may be associated with the purported ω Cen debris stream. Many of these stars exhibit enhanced [Ba/Fe]

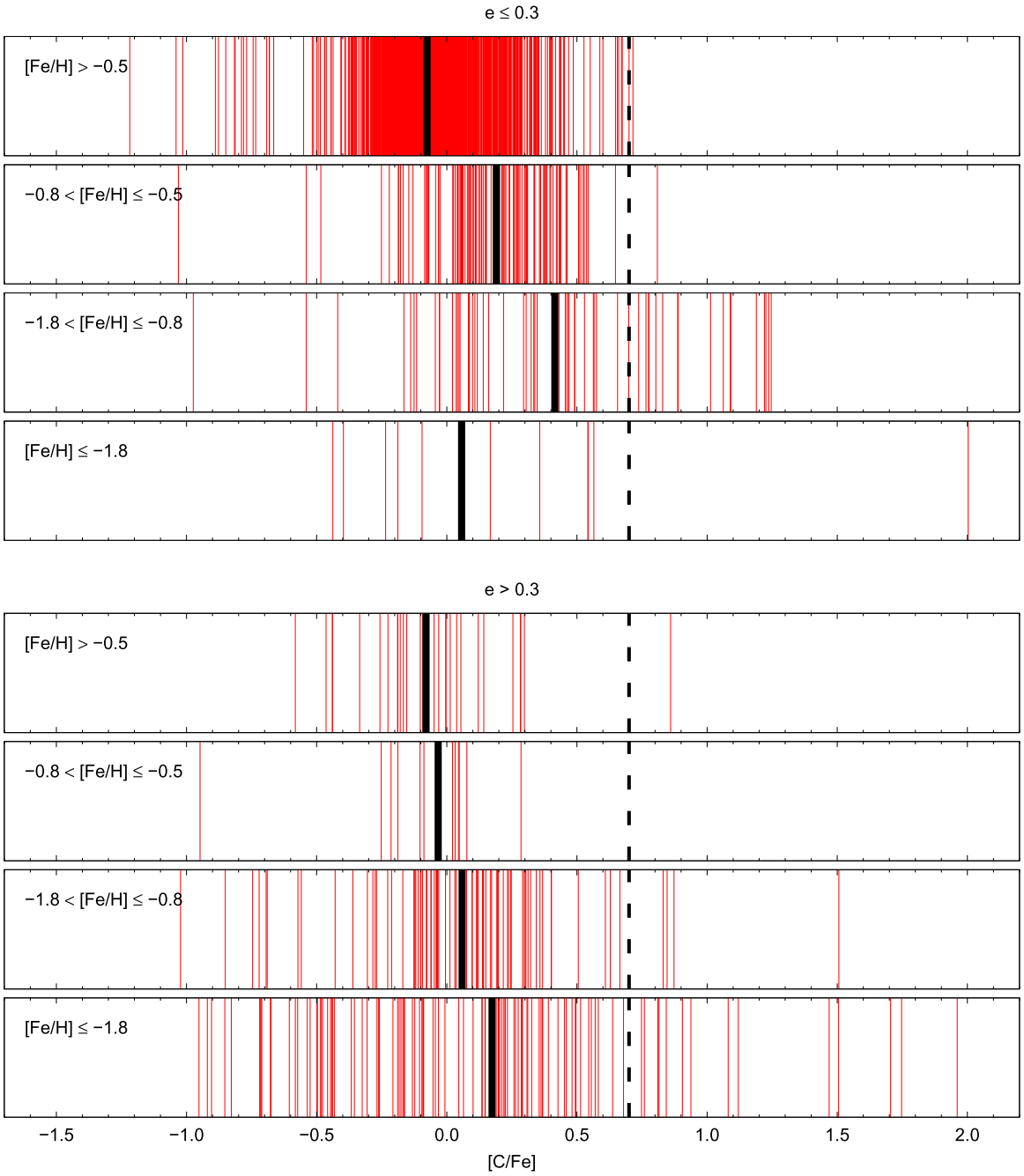

Figure 15. Stripe-density diagrams of the carbonicity [C/Fe] for stars in the combined sample. The plots are split into low-eccentricity ($e \leqslant 0.3$; upper panels) and high-eccentricity ($e > 0.3$; lower panels) sub-samples. Each sub-sample is further divided into metallicity intervals chosen to separate regions dominated by individual components of the disk and halo systems. See text for more details. The black stripes indicate the mean [C/Fe] for the stars in each subset. The vertical dashed line indicates the level of carbon enhancement used in this paper to indicate CEMP stars, [C/Fe] $> +0.7$. Note the relatively high fraction of CEMP stars among the low-eccentricity stars with metallicities $-1.8 <$ [Fe/H] $\leqslant -0.8$, which are likely members of the MWTD. Stars with errors exceeding 50 km s^{-1} in any of the individual derived components of motion are excluded.

ratios, similar to those of CEMP-*s* stars previously identified in the cluster. Given the relative rarity of CEMP stars found in most globulars, they considered this compelling evidence that the field stars they identified were indeed once associated with ω Cen. The one CEMP-*s* and four CEMP-no stream stars in our sample all have [Fe/H] < -2, falling below the lower-metallicity range associated with ω Cen (Frinchaboy et al. 2002). As indicated in the table, 14 of the listed stars have existing high-resolution spectroscopy (most unpublished, from our group). We are in the process of obtaining high-resolution spectroscopy for the stars in this table that presently lack this information; the full sample will be described in due course.

5. CARBON-ENHANCED METAL-POOR STARS IN THE COMBINED SAMPLE

Figure 13 shows the distribution of carbonicity [C/Fe] as a function of [Fe/H] for the stars in the combined sample. The general increase in the level of [C/Fe] with decreasing [Fe/H]

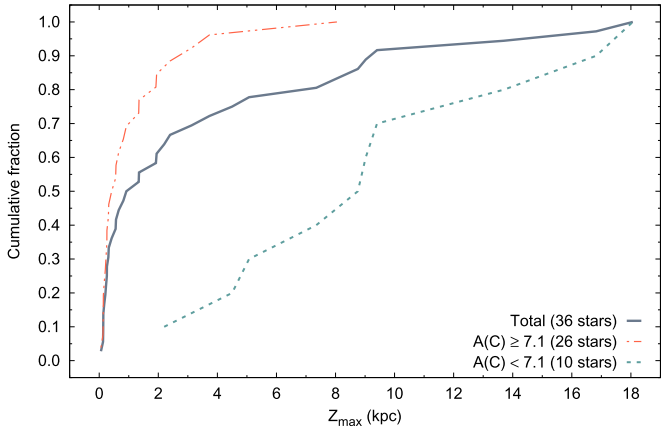

Figure 16. Cumulative fractions of CEMP stars as a function of Z_{max} for stars with [Fe/H] $\leqslant -2.0$ in the combined sample with available measurements. The solid line applies to the full sample, which has a total of 36 CEMP stars. The blue dashed line applies to the 26 CEMP stars with absolute carbon abundance $A(C) \geqslant 7.1$, while the red dashed line applies to those with $A(C) < 7.1$, a division suggested by Yoon et al. (2016) to distinguish CEMP-*s* stars from CEMP-no stars. Note the clear difference in the behavior of these two subsets. See text for more details. Stars with errors exceeding 50 km s^{-1} in any of the individual derived components of motion are excluded.

is clearly evident, as is the increase in the frequency of CEMP stars with decreasing metallicity below [Fe/H] $= -1.0$, as has been seen in numerous previous studies. Note that our present study, following most recent work, employs the criterion [C/Fe] $> +0.7$ (rather than [C/Fe] $> +1.0$, commonly used previously) to identify CEMP stars. It is interesting to note the similarity of this figure to that reported by Rossi et al. (1999; their Figure 2), who made these same points (as did Norris et al. 1997) almost twenty years ago.

One early claim on the existence of an increased fraction of CEMP stars with [Fe/H] $\leqslant -2.0$, 9%, was made by Paper I; this fraction is somewhat lower than those reported by Beers et al. (1992; ∼14%) and by authors of contemporaneous studies (e.g., Beers & Christlieb 2005; Cohen et al. 2005; Marsteller et al. 2005; Lucatello et al. 2006; ∼15%–20%). All such estimates were, however, based on relatively small samples and did not account for the depletion of carbon for stars in advanced evolutionary stages.

Figure 14 shows the distribution of cumulative frequencies for CEMP stars in our combined sample as a function of [Fe/H]. Although the total number of CEMP stars in our sample is still small ($N = 52$), compared to those in more recent work (e.g., Lee et al. 2013; Placco et al. 2014), the behavior is similar. For completeness, we note that we obtain cumulative frequencies of CEMP stars of $19\% \pm 4\%$ for stars with [Fe/H] $\leqslant -2.0$, $24\% \pm 6\%$ for stars with [Fe/H] $\leqslant -2.5$, and $39\% \pm 15\%$ for stars with [Fe/H] $\leqslant -3.0$. These numbers compare well with the cumulative frequencies of CEMP stars as a function of decreasing metallicity from Lee et al. (2013) but are somewhat lower than the frequencies reported in Placco et al. (2014), an analysis that was based exclusively on stars with results from high-resolution spectroscopic analyses, particularly if one considers the results after corrections for the depletion of carbon in more-evolved stars.

It is interesting to consider the distribution of carbonicity for stars in our combined sample in different ranges of orbital eccentricity, shown in Figure 15. It should be recalled that this sample only includes stars with well-measured kinematics. Note that the low-eccentricity stars shown on the upper panels of this figure possess only a few stars that exceed [C/Fe] $= +0.7$ (and hence are considered CEMP stars), and all but a few of those are found in the metallicity range $-1.8 <$ [Fe/H] $\leqslant -0.8$ that is expected to apply to the MWTD population. The relatively large fraction of CEMP stars that may belong to the MWTD has implications for its formation, but larger samples of stars and more detailed modeling are required before a definitive evaluation can be made. The high-eccentricity stars on the lower panels include a few stars in the same metallicity range, but most are probably associated with the inner-halo population. The majority of the high-eccentricity CEMP stars are found in the metallicity range [Fe/H] $\leqslant -1.8$ that is expected to include members from both the inner- and outer-halo populations.

As noted above, Paper I made the first published claim that there exists an increasing frequency of CEMP stars with distance from the Galactic plane (although most of the weight for this suggestion came from the addition of stars from the sample of Beers et al. 1992). Carollo et al. (2012) confirmed and extended this claim using a much larger sample of stars from SDSS. Here, we examine this question once again, using our combined sample.

The solid black line shown in Figure 16 shows the cumulative fractions of CEMP stars with [Fe/H] $\leqslant -2.0$ in our combined sample as a function of Z_{max}, which clearly support the original claim from Paper I. This figure also shows lines representing stars from this sample divided by their absolute carbon abundance at $A(C) \geqslant 7.1$ (red dotted–dashed line) or $A(C) < 7.1$ (blue dashed line), the level suggested by Yoon et al. (2016) to effectively separate CEMP-*s* stars (those above this value) from CEMP-no stars (those below this value). Although the number of CEMP stars under consideration is still small (as indicated in the legend of the figure), there is a rather dramatic contrast seen between the high-A(C) and low-A(C) stars, commensurate with expectation from the study by Carollo et al. (2014) that the inner-halo population of stars is comprised of a larger fraction of CEMP-*s* stars than the outer-halo population, which includes relatively greater numbers of CEMP-no stars. A similar exercise applied to the SDSS sample of CEMP stars, now underway, should prove illuminating.

For convenience and to inspire future high-resolution spectroscopic study and radial velocity monitoring of the relatively bright CEMP stars we have identified in this work, we list in Table 8 the full set of these stars in our combined sample. Column (1) provides the star names, column (2) lists their coordinates, and columns (3) and (4) list the V and $B - V$ colors, respectively. Column (5) lists the derived metallicity [Fe/H]$_C$. Columns (6) and (7) list the carbonicity [C/Fe]$_C$ and absolute carbon abundances A(C), respectively. The sub-classification of these CEMP stars, obtained by application of the Yoon et al. (2016) separation of CEMP-*s* stars from CEMP-no stars, is listed in column (8). Stars for which a high-resolution spectrum presently exists (roughly half of the stars, mostly unpublished, from our group) are indicated in the table.

Note that a couple of *known* CEMP stars that are included in our sample, HE 1327-2326 and HE 1337-0012 (G 64-12), are not included in this table, since they are sufficiently warm that carbon enhancement could not be demonstrated based on the medium-resolution spectroscopy we have reported in this paper. There are likely to be others; see the discussion by Placco et al. (2016) of the CEMP status of G 64-12 and G 64-37. Furthermore, due to the large errors in estimated surface

Table 8
CEMP Stars and Their Sub-classifications in the Combined Sample

Star Name (1)	R.A. (2000) Decl. (2)	V (3)	$B-V$ (4)	$[Fe/H]_C$ (5)	$[C/Fe]_C$ (6)	A(C) (7)	Class (8)
HE 0013-0257[a]	00 16 04.2 −02 41 05	12.71	0.79	−3.42	0.75	5.76	CEMP-no
HE 0015-0048[a]	00 18 01.4 +01 05 08	13.20	0.76	−2.70	0.81	6.54	CEMP-no
HE 0027-1221[a]	00 30 31.1 −12 05 11	13.03	0.67	−2.50	2.55	8.47	CEMP-*s*
HE 0030-5441	00 33 20.1 −54 24 43	10.62	0.36	−1.26	0.77	7.94	CEMP-*s*
HE 0038-0345	00 41 09.3 −03 29 00	11.42	0.78	−2.66	0.76	6.53	CEMP-no
HE 0039-2635[a]	00 41 39.8 −26 18 54	12.18	1.15	−3.94	3.15	7.64	CEMP-*s*
HE 0054-2542[a]	00 57 18.1 −25 26 10	12.63	0.95	−3.52	2.63	7.54	CEMP-*s*
HE 0058-3449	01 01 21.7 −34 33 11	13.21	0.71	−2.22	0.96	7.17	CEMP-*s*
HE 0228-0149	02 30 56.0 −01 36 03	12.68	0.51	−1.79	0.87	7.52	CEMP-*s*
BM-024[a]	02 39 02.5 −49 27 46	10.11	0.77	−2.52	1.71	7.62	CEMP-*s*
HE 0247-0254	02 50 16.9 −02 41 50	13.38	0.60	−1.49	1.51	8.45	CEMP-*s*
BM-043[a]	04 13 13.1 +06 36 02	9.10	1.29	−2.46	2.43	8.40	CEMP-*s*
HE 0412-0138	04 15 33.5 +01 45 58	10.50	0.75	−1.52	0.78	7.69	CEMP-*s*
HE 0414-0343[a]	04 17 16.5 −03 36 31	10.63	1.09	−3.23	1.75	6.95	CEMP-*s*
HE 0420-0123[a]	04 23 14.5 +01 30 48	11.35	0.79	−2.75	2.47	8.15	CEMP-*s*
HE 0440-3426[a]	04 42 08.2 −34 21 14	11.42	1.18	−2.46	1.12	7.09	CEMP-no
HE 0448-4806[a]	04 49 33.1 −48 01 08	12.78	0.62	−2.76	2.88	8.55	CEMP-*s*
HE 0543-5350	05 44 42.0 −53 49 01	11.97	0.48	−2.39	0.88	6.92	CEMP-*s*
BM-074	06 04 07.1 −20 37 14	8.69	0.48	−1.01	1.01	8.43	CEMP-*s*
BM-083	06 34 55.5 −45 18 30	7.19	0.81	−2.12	0.94	7.25	CEMP-*s*
BM-091	07 34 28.9 −13 52 13	6.70	0.47	−1.24	1.09	8.28	CEMP-*s*
HE 0900-0001	09 02 41.3 −00 13 35	12.70	0.39	−1.64	1.09	7.88	CEMP-*s*
BM-107	09 23 02.1 −49 03 31	8.89	0.33	−1.01	0.88	8.30	CEMP-*s*
HE 0920-0506	09 23 06.0 −05 19 33	11.50	0.68	−1.39	1.19	8.23	CEMP-*s*
HE 1109-0025	11 12 06.7 −00 41 30	10.64	0.45	−1.25	1.06	8.24	CEMP-*s*
HE 1114-2757	11 17 00.8 −28 14 12	10.47	0.62	−1.27	0.85	8.00	CEMP-*s*
HE 1119-0218	11 22 27.0 +02 02 10	11.39	0.50	−1.44	1.22	8.21	CEMP-*s*
HE 1143-0114[a]	11 46 31.7 +00 57 30	12.42	0.53	−2.44	2.50	8.50	CEMP-*s*
HE 1154-2951[a]	11 56 39.4 −30 08 31	10.49	0.45	−2.54	2.00	7.90	CEMP-*s*
HE 1225-0155[a]	12 28 04.8 +01 38 33	12.95	0.74	−2.68	0.77	6.52	CEMP-no
HE 1243-2408[a]	12 45 54.1 −24 24 46	10.85	0.81	−2.84	0.75	6.34	CEMP-no
HE 1300-2739	13 03 19.8 −27 55 54	10.19	0.72	−1.63	0.89	7.69	CEMP-*s*
HE 1327-2116[a]	13 30 19.4 −21 32 03	11.59	1.11	−3.48	2.64	7.59	CEMP-*s*
HE 1350-2955	13 53 05.7 −30 10 11	10.36	0.49	−1.14	0.83	8.12	CEMP-*s*
HE 1403-2207	14 06 41.5 −22 21 23	9.74	0.22	−1.16	0.78	8.05	CEMP-*s*
HE 1410-0125	14 13 24.8 −01 39 53	12.61	1.25	−2.87	1.47	7.03	CEMP-no
HE 1412-0847	14 14 57.4 −09 01 45	12.58	0.60	−1.81	1.96	8.58	CEMP-*s*
HE 1457-1215[a,b]	15 00 30.9 −12 26 57	10.18	0.55	−1.56	1.23	8.09	CEMP-*s*
BM-218	15 47 47.9 −57 48 30	8.93	0.65	−1.43	0.77	7.77	CEMP-*s*
BM-285[a]	21 06 02.9 −61 33 45	9.81	0.73	−2.12	0.84	7.15	CEMP-*s*
BM-287	21 09 04.6 −55 17 36	8.35	0.34	−1.17	1.24	8.50	CEMP-*s*
HE 2138-0314[a]	21 40 41.6 −03 01 17	13.23	0.57	−3.07	0.91	6.27	CEMP-no
HE 2155-2043[a]	21 58 42.3 −20 29 16	13.19	0.75	−3.27	0.81	5.97	CEMP-no
HE 2214-1654[a]	22 17 01.7 −16 39 27	13.19	0.81	−3.60	1.08	5.91	CEMP-no[c]
BM-309	22 37 51.0 −60 05 41	8.69	0.43	−1.00	0.74	8.17	CEMP-*s*
HE 2235-5058[a]	22 38 08.0 −50 42 41	12.92	0.92	−3.81	3.16	7.78	CEMP-*s*
HE 2240-1647	22 42 57.0 −16 31 20	12.68	0.78	−3.18	1.51	6.75	CEMP-no
HE 2250-4229[a]	22 53 39.7 −42 13 04	11.91	0.75	−2.83	0.82	6.42	CEMP-no
HE 2319-5228[a]	23 21 58.2 −52 11 43	13.25	0.90	−3.39	1.47	6.51	CEMP-no
HE 2342-3815	23 45 08.3 −37 59 15	11.10	0.36	−1.12	0.83	8.14	CEMP-*s*
HE 2343-1817	23 46 14.7 −18 00 47	11.90	0.64	−2.14	2.09	8.38	CEMP-*s*

Notes.
[a] A high-resolution spectrum exists for this star.
[b] This star is also BM-209.
[c] This star is a rediscovery of CS 22892-052, a known CEMP-*r* star.

gravities from our medium-resolution analysis (∼0.5 dex), we have not explicitly applied corrections for the depletion of carbon for stars in advanced evolutionary stages (Placco et al. 2014). There are a total of 43 stars in our combined sample with surface gravity estimates log $g < 2.0$, where corrections can become significant. Of these, seven stars (HE 0013-0522, HE 0111-1118, HE 0117-0201, HE 0147-4926, HE 1313-1916, HE 2243-0244, and BM-005 = HD 4306) would be considered CEMP stars if corrections were applied. Further attention to these stars is clearly warranted.

6. SUMMARY AND DISCUSSION

We have re-analyzed spectra from a previously published sample of 1777 bright metal-poor candidates from the HES (Frebel et al. 2006) and obtained new estimates of their atmospheric parameters $T_{\rm eff}$, log g, and [Fe/H], as well as the carbonicity [C/Fe]. A large number of stars (those with [Fe/H] > -1.0) whose parameters could not be estimated previously with the tools in hand are included in our results. The carbonicity estimates are refined as well, based on a new grid of carbon-enhanced synthetic spectra. We combine this sample with stars from the "weak metal" candidates of Bidelman & MacConnell (1973), which were analyzed in a similar fashion by Beers et al. (2014), obtaining a total sample of 2079 stars. We present a chemodynamical analysis of 1892 stars from this combined sample with suitably precise derived kinematic properties and identify new stars that appear to be associated with the previously suggested halo debris streams from Helmi et al. (1999) and Chiba & Beers (2000), as well as with debris stripped from the globular cluster ω Cen, discussed by Dinescu (2002) and Majewski et al. (2012).

It is interesting that a number of the lowest-metallicity stars we identify as part of the ω Cen debris stream are CEMP-no stars, which are not expected to form in globular clusters. This may lend credence to previous speculations that the globular cluster ω Cen may have been stripped from a parent dwarf galaxy. If one assumes that this is the case, this meets expectations based on the analysis of other debris streams, such as the Sagittarius Stream, where a number of authors (e.g., de Boer et al. 2015) have suggested that the low-metallicity stars associated with the parent dwarf were less bound than the higher-metallicity stars and were stripped early in its interaction with the Milky Way. Further study of the individual stars, which we suggest may be associated with the putative parent dwarf of ω Cen, is clearly necessary before this possibility can be confirmed.

We identify a clear increase in the cumulative frequency of CEMP stars with declining metallicity as well as an increase in the fraction of CEMP stars with distance from the Galactic plane, consistent with previous results. We also identify a relatively large number of CEMP stars with kinematics consistent with those of the MWTD population. This may be understood if the MWTD were, at least in part, assembled from the debris of low-mass dwarf galaxies, where CEMP stars (especially CEMP-no stars) are expected to have formed at high frequency. Although the small number of stars in this sample precludes stronger conclusions, it will be interesting to look for this signature in surveys that include larger samples of likely MWTD stars.

Finally, the 61 CEMP stars in our combined sample are sub-classified into likely CEMP-*s* and CEMP-no stars using the absolute carbon abundances A(C), as suggested recently by Yoon et al. (2016).

High-resolution spectroscopic analyses of our program stars in the debris streams that lack this information as well as those identified as CEMP stars are now underway and will be reported in due course. Since these stars are among the brightest known examples of the CEMP phenomenon, long-term radial velocity monitoring of these stars, now underway, should provide valuable information concerning their likely progenitors.

T.C.B., D.C., V.M.P., and S.D. acknowledge partial support for this work from grants PHY 08-22648, Physics Frontier Center/JINA, and PHY 14-30152, Physics Frontier Center/JINA Center for the Evolution of the Elements, awarded by the US National Science Foundation. S.R. acknowledges partial support for this work from CAPES, CNPq, FAPESP, and INCT. Y.S.L. acknowledges partial support from the National Research Foundation of Korea (NRF) to the Center for Galaxy Evolution Research and Basic Science Research Program, funded by the Ministry of Science, ICT, and Future Planning (NRF-2015R1C1A1A02036658). A.F. acknowledges funding from NSF-CAREER grant AST 12-55160 and from the Silverman (1968) Family Career Development Professorship. The study at RSAA, ANU, of the Galaxy's metal-poor stars is supported by Australian Research Council grants DP0663562 and DP0984924, which J.E.N. is pleased to acknowledge.

REFERENCES

Allende Prieto, C., Sivarani, T., Beers, T. C., et al. 2008, AJ, 136, 2070
Aoki, W., Frebel, A., Christlieb, N., et al. 2006, ApJ, 639, 897
Asplund, M., Grevesse, N., Sauval, A. J., & Scott, P. 2009, ARA&A, 47, 481
Beers, T. C., Carollo, D., Ivezić, Ž., et al. 2012, ApJ, 746, 34
Beers, T. C., Chiba, M., Yoshii, Y., et al. 2000, AJ, 119, 2866
Beers, T. C., & Christlieb, N. 2005, ARA&A, 43, 531
Beers, T. C., Flynn, C., Rossi, S., et al. 2007, ApJS, 168, 128
Beers, T. C., Norris, J. E., Placco, V. M., et al. 2014, ApJ, 794, 58
Beers, T. C., Preston, G. W., & Shectman, S. A. 1985, AJ, 90, 2089
Beers, T. C., Preston, G. W., & Shectman, S. A. 1992, AJ, 103, 1987
Beers, T. C., Rossi, S., Norris, J. E., Ryan, S. G., & Shefler, T. 1999, AJ, 117, 981
Bessell, M. S., Collet, R., Keller, S. C., et al. 2015, ApJL, 806, L16
Bidelman, W. P., & MacConnell, D. J. 1973, AJ, 78, 687
Bovy, J., Rix, H.-W., Liu, C., et al. 2012, ApJ, 753, 148
Bovy, J., Rix, H.-W., Schlafly, E. F., et al. 2015, ApJ, 823, 30
Carollo, D., Beers, T. C., Bovy, J., et al. 2012, ApJ, 744, 195
Carollo, D., Beers, T. C., Chiba, M., et al. 2010, ApJ, 712, 692
Carollo, D., Beers, T. C., Lee, Y. S., et al. 2007, Natur, 450, 1020
Carollo, D., Freeman, K., Beers, T. C., et al. 2014, ApJ, 788, 180
Chiba, M., & Beers, T. C. 2000, AJ, 119, 2843
Christlieb, N. 2003, RvMP, 16, 191
Cohen, J. G., Shectman, S., Thompson, I., et al. 2005, ApJL, 633, L109
de Boer, T. J. L., Belokurov, V., & Koposov, S. 2015, MNRAS, 451, 3489
Dinescu, D. I. 2002, in ASP Conf. Proc. 265, Omega Centauri, A Unique Window into Astrophysics, ed. F. van Leeuwen et al. (San Francisco, CA: ASP), 365
Frebel, A. 2010, AN, 331, 474
Frebel, A., Aoki, W., Christlieb, N., et al. 2005, Natur, 434, 871
Frebel, A., Christlieb, N., Norris, J. E., et al. 2006, ApJ, 652, 1585 (Paper I)
Frinchaboy, P. M., Rhee, J., Ostheimer, J. C., et al. 2002, in ASP Conf. Proc. 265, Omega Centauri, A Unique Window into Astrophysics, ed. F. van Leeuwen et al. (San Francisco, CA: ASP), 143
Ghez, A. M., Salim, S., Weinberg, N. N., et al. 2008, ApJ, 689, 1044
Gilmore, G., Randich, S., Asplund, M., et al. 2012, Msngr, 147, 25
Girard, T. M., van Altena, W. F., Zacharias, N., et al. 2011, AJ, 142, 15
Guiglion, G., Recio-Blanco, A., de Laverny, P., et al. 2015, A&A, 583, 91

Helmi, A., White, S. D. M., de Zeeuw, P. T., & Zhao, H. S. 1999, Natur, 402, 53
Henden, A. A., Levine, S., Terrell, D., & Welch, D. L. 2015, BAAS, 225, 336.16
Høg, E., Fabricius, C., Makarov, V. V., et al. 2000, A&A, 355, L27
Kawata, D., & Chiappini, C. 2016, AN, 337, 96
Keller, S. C., Bessell, M. S., Frebel, A., et al. 2014, Natur, 506, 463
Kerr, F. J., & Lynden-Bell, D. 1986, MNRAS, 221, 1023
Klement, R., Rix, H.-W., Flynn, C., et al. 2009, ApJ, 698, 865
Koposov, S. E., Yoo, J., Rix, H.-W., et al. 2009, ApJ, 696, 2179
Kordopatis, G., Gilmore, G., Steinmetz, M., et al. 2013, AJ, 146, 134
Lee, Y. S., Beers, T. C., Allende Prieto, C., et al. 2011a, AJ, 141, 90
Lee, Y. S., Beers, T. C., An, D., et al. 2011b, ApJ, 738, 187
Lee, Y. S., Beers, T. C., Masseron, T., et al. 2013, AJ, 146, 132
Lee, Y. S., Beers, T. C., Sivarani, T., et al. 2008a, AJ, 136, 2022
Lee, Y. S., Beers, T. C., Sivarani, T., et al. 2008b, AJ, 136, 2050
Lucatello, S., Beers, T. C., Christlieb, N., et al. 2006, ApJL, 652, L37
Majewski, S. R., Nidever, D. L., Smith, V. V., et al. 2012, ApJL, 747, L37
Majewski, S. R., Schiavon, R. P., Frinchaboy, P. M., et al. 2015, AJ, submitted (arXiv:1509.04520)
Marsteller, M., Beers, T. C., Rossi, S., et al. 2005, NuPhA, 758, 312
Mihalas, D., & Binney, J. 1981, Galactic Astronomy: Structure and Kinematics (2nd ed.; San Francisco: Freeman)
Norris, J. E., Bessell, M. S., & Pickles, A. J. 1985, ApJS, 58, 463
Norris, J. E., Ryan, S. G., & Beers, T. C. 1997, ApJ, 488, 350
Placco, V. M., Beers, T. C., Reggiani, H., & Melendez, J. 2016, ApJL, 829, L24
Placco, V. M., Frebel, A., Beers, T. C., & Stancliffe, R. 2014, ApJ, 797, 21
Rossi, S., Beers, T. C., & Sneden, C. 1999, in ASP Conf. Ser. 165, The Third Stromlo Symp.: The Galactic Halo, ed. B. K. Gibson, T. S. Axelrod, & M. E. Putman (San Francisco, CA: ASP), 264
Santucci, R. M., Placco, V. M., Rossi, S., et al. 2015, ApJ, 801, 116
Schlegel, D. J., Finkbeiner, D. P., & Davis, M. 1998, ApJ, 500, 525
Skrutskie, M. F., Cutri, R. M., Stiening, R., et al. 2006, AJ, 131, 1163
Smolinski, J. P., Lee, Y. S., Beers, T. C., et al. 2011, AJ, 141, 89
Soubiran, C., Le Campion, J.-F., Brouillet, N., & Chemin, L. 2016, A&A, 591, 118
Soubiran, C., Le Campion, J.-F., Cayrel de Strobel, G., & Caillo, A. 2010, A&A, 515, 111
Steinmetz, M., Zwitter, T., Siebert, A., et al. 2006, AJ, 132, 1645
Suda, T., Katsuta, Y., Yamada, S., et al. 2008, PASJ, 60, 1159
Suda, T., Yamada, S., Katsuta, Y., et al. 2011, MNRAS, 412, 843
van Leeuwen, F. 2007, A&A, 474, 653
Wisotzki, L., Christlieb, N., Bade, N., et al. 2000, A&A, 358, 77
Yamada, S., Suda, T., Komiya, Y., Aoki, W., & Fujimoto, M. Y. 2013, MNRAS, 436, 1362
Yanny, B., Rockosi, C., Newberg, H. J., et al. 2009, AJ, 137, 4377
Yoon, J., Beers, T. C., Placco, V. M., et al. 2016, ApJ, 833, 20
York, D. G., Adelman, J., Anderson, J. E., et al. 2000, AJ, 120, 1579
Zacharias, N., Finch, C. T., Girard, T. M., et al. 2013, AJ, 145, 44